



# The impact of evaporation fractionation on the inverse estimation of soil hydraulic and isotope transport parameters

Tiantian Zhou, Jirka Šimůnek, Isabelle Braud, Paolo Nasta, Giuseppe Brunetti, Yi Liu

## ► To cite this version:

Tiantian Zhou, Jirka Šimůnek, Isabelle Braud, Paolo Nasta, Giuseppe Brunetti, et al.. The impact of evaporation fractionation on the inverse estimation of soil hydraulic and isotope transport parameters. Journal of Hydrology, 2022, 612, pp.128100. 10.1016/j.jhydrol.2022.128100 . hal-03740651

**HAL Id: hal-03740651**

**<https://hal.inrae.fr/hal-03740651>**

Submitted on 29 Jul 2022

**HAL** is a multi-disciplinary open access archive for the deposit and dissemination of scientific research documents, whether they are published or not. The documents may come from teaching and research institutions in France or abroad, or from public or private research centers.

L'archive ouverte pluridisciplinaire **HAL**, est destinée au dépôt et à la diffusion de documents scientifiques de niveau recherche, publiés ou non, émanant des établissements d'enseignement et de recherche français ou étrangers, des laboratoires publics ou privés.



Distributed under a Creative Commons Attribution - NonCommercial - NoDerivatives 4.0 International License

**Publisher:** Elsevier

**Journal:** Journal of Hydrology

**DOI:** 10.1016/j.jhydrol.2022.128100

## **The impact of evaporation fractionation on the inverse estimation of soil hydraulic and isotope transport parameters**

Tiantian Zhou<sup>1\*</sup>, Jirka Šimůnek<sup>1\*</sup>, Isabelle Braud<sup>2</sup>, Paolo Nasta<sup>3</sup>, Giuseppe Brunetti<sup>4</sup>, and Yi Liu<sup>5</sup>

<sup>1</sup> Department of Environmental Sciences, University of California Riverside, CA 92521, United States

<sup>2</sup> INRAE, Riverly, 5 Rue de la Doua, 69625 Villeurbanne, Cedex, France

<sup>3</sup> Department of Agricultural Sciences, AFBE Division, University of Naples Federico II, Portici (Naples), Italy

<sup>4</sup> Institute of Hydraulics and Rural Water Management, University of Natural Resources and Life Sciences, 1190, Vienna, Austria

<sup>5</sup> China Institute of Geo-Environment Monitoring, China Geological Survey, Beijing, 100081, China

Corresponding author: email: [tzhou035@ucr.edu](mailto:tzhou035@ucr.edu); [jiri.simunek@ucr.edu](mailto:jiri.simunek@ucr.edu)

## **Abstract**

Choosing a suitable process-oriented eco-hydrological model is essential for obtaining reliable simulations of hydrological processes. Determining soil hydraulic and solute transport parameters is another fundamental prerequisite. Research discussing the impact of considering evaporation fractionation on parameter estimation and practical applications of isotope transport models is limited. In this study, we analyzed parameter estimation results for two datasets for humid and arid conditions using the isotope transport model in HYDRUS-1D, in which we either did or did not consider fractionation. The global sensitivity analysis using the Morris and Sobol' methods and the parameter estimation using the Particle Swarm Optimization algorithm highlight the significant impact of considering evaporation fractionation on inverse modeling. The Kling-Gupta efficiency (KGE) index for isotope data can increase by 0.09 and 1.49 for the humid and arid datasets, respectively, when selecting suitable fractionation scenarios. Differences in estimated parameters propagate into the results of two practical applications of stable isotope tracing: *i*) the assessment of root water uptake (RWU) and drainage travel times (i.e., the time elapsed between water entering the soil profile as precipitation and leaving it as transpiration or drainage) in the lysimeter (humid conditions) and *ii*) evaporation estimation in a controlled experimental soil column (arid conditions). The peak displacement method with optimized longitudinal dispersivity provides much lower travel times than those obtained using the particle tracking algorithm in HYDRUS-1D. Considering evaporation fractionation using the Craig-Gordon (CG) and Gonfiantini models is likely to result in estimates of older water ages for RWU than the no fractionation scenario. The isotope mass balance method that uses the isotopic composition profile simulated by HYDRUS-1D while considering fractionation using the CG and Gonfiantini models, or the measured evaporation isotope flux, provides comparable results in evaporation estimation as the HYDRUS-1D water mass balance method and direct laboratory measurements. In contrast,

the no fractionation scenario reasonably estimates evaporation only when using the HYDRUS-1D water mass balance method. The direct use of simulated isotopic compositions in the no fractionation scenario may result in large biases in practical applications in the arid zone where evaporation fractionation is more extensive than in humid areas.

**Keywords:** HYDRUS-1D, Global sensitivity analysis; Particle swarm optimization; Water travel time, Temporal origin, Evaporation estimation

## 1 Introduction

Reliable water balance simulations in the vadose zone are important to understand and forecast the impact of anthropogenic disturbances such as global warming and land-use change on soil water storage, groundwater recharge, and evapotranspiration. A detailed mechanistic understanding of water fluxes in the vadose zone could support optimal and efficient management strategies for promoting the long-term sustainability of water resources and associated ecosystem functions (Penna et al., 2018). For example, the exact quantification of evaporation affects water availability for plants (Nelson et al., 2020) and constrains groundwater recharge (Condon et al., 2020). However, the conventional methods (e.g., pan experiments) for estimating evaporation fluxes often require extensive field monitoring of water flow, which is often time-consuming, expensive, labor-demanding, and affected by considerable uncertainty (Skrzypek et al., 2015).

Stable isotopes of hydrogen ( $^2\text{H}$ ) and oxygen ( $^{18}\text{O}$ ) are widely used to trace water fluxes across the critical zone and can be expressed as isotopic ratios,  $^2\text{H}/^1\text{H}$  and  $^{18}\text{O}/^{16}\text{O}$  by using the  $\delta$  notation (i.e.,  $\delta^2\text{H}$  and  $\delta^{18}\text{O}$ ). The isotopic composition of shallow soil water provides insights into evaporation fractionation characteristics. This information can be easily used to calculate corresponding evaporation fluxes. For example, Skrzypek et al. (2015) combined the equations for evaporation estimation based on the revised Craig-Gordon model (Craig and Gordon, 1965) and developed a software Hydrocalculator. Using this software, they estimated evaporation losses and validated its results using pan measurements. This method has been extended to soil evaporation estimation. For example, Sprenger et al. (2017) estimated that evaporation was about 5 and 10% of infiltrating water in the heath and Scots pine soils, respectively.

While the spatial origin of the water plants use has been widely studied (e.g., Allen et al., 2019), very little is known about its temporal origin (Brinkmann et al., 2018; Miguez-Macho and Fan, 2021). To

track water across the critical zone, we need to assess how fast water moves down to the soil profile bottom and when and how much water returns to the atmosphere through root water uptake (RWU). The premise is to accurately estimate travel times (TT) of irrigation/precipitation water (i.e., the time between water entering the soil profile as irrigation/precipitation and leaving it back to the atmosphere as transpiration or at the soil profile bottom as drainage).

The peak displacement method represents the most widespread technique to estimate travel time from the time difference between signals in soil water stable isotope time-series directly measured at specific soil depths (Chesnaux and Stumpp, 2018; Koeniger et al., 2016; Stumpp et al., 2012). However, this method is unfeasible when there is no pronounced peak correspondence between isotopic compositions of precipitation and drainage water samples. Another widely-used isotope-transport-based method is to inversely estimate the parameters for time-invariant TT distributions (TTDs) (e.g., Timbe et al., 2014) or time-variant StorAge Selection (SAS) functions (Benettin and Bertuzzo, 2018; Harman, 2015; Rinaldo et al., 2015) implemented in lumped hydrological models. Such oversimplified models are based on few soil and vegetation parameters but have limitations in describing transient conditions or simulating isotope transport (Sprenger et al., 2016a).

In contrast, isotope transport can be reliably simulated using the Richards equation-based hydrological models with appropriate soil and vegetation parameters and known boundary and initial conditions. However, direct measurements of soil hydraulic and transport parameters required by such models are time-consuming and labor-demanding. Therefore, such parameters are commonly obtained using inverse modeling by minimizing the errors between easily-measured state variables and fluxes (e.g., soil water contents and pressure heads at different soil depths or leachate water volumes) and corresponding model simulations (Hopmans et al. 2002; Mertens et al., 2006; Vrugt et al., 2008; Wollschläger et al., 2009; Wöhling and Vrugt, 2011).

Nevertheless, it is not always necessary to account for all model parameters in parameter optimization since some can be fixed as they can be either determined experimentally or have a minor impact

on the model output. The latter can be determined using the global sensitivity analysis (GSA). The Sobol' and Morris methods are among the two most widespread GSA methods (Liu et al., 2020). The Sobol' method provides the most accurate sensitivity indices, but it requires several model runs and is thus computationally intensive (Gatel et al., 2019). In contrast, the Morris method cannot yield the order of the most sensitive parameters as accurately as the Sobol' method, but its computational cost is much lower, and it can still pinpoint the most influential parameters (Campolongo et al., 2007; Herman et al., 2013).

Many inverse modeling algorithms can be used for parameter estimation. For example, the Levenberg-Marquardt Optimization (LMO) proved to be very efficient and was, therefore, implemented in HYDRUS (Šimůnek et al., 2008). However, the LMO is sensitive to the initial parameter values provided by the user and often falls into local instead of global minimum (Brunetti et al., 2016). Thus, global optimization algorithms, such as Particle Swarm Optimization (PSO), have become more widespread over the last decades (e.g., Vrugt and Robinson, 2007).

When optimizing isotope transport parameters via inverse modeling, isotopic compositions from multiple soil depths must be included in the objective function and combined with other state variables and fluxes. For example, research shows that the model calibration can be improved by simultaneously considering stable isotopes and soil moisture information (Sprenger et al., 2015; Groh et al., 2018; Mattei et al., 2020). However, the correct model structure is a fundamental prerequisite to obtaining successful simulations. In particular, research discussing the impact of considering evaporation fractionation on parameter estimation and practical applications of isotope transport models is limited (Penna et al., 2018). Therefore, we pose two scientific questions. First, how will the consideration of evaporation fractionation affect the parameter estimation results of the isotope transport model? Second, how will this effect propagate into practical applications such as water travel times and evaporation estimation?

To answer these questions, we compare the parameter estimation results obtained using the isotope transport model in HYDRUS-1D (Zhou et al., 2021) that does or does not consider evaporation fractionation for two available datasets: 1) a 150-cm-thick layered soil profile in a lysimeter under humid climate where

evaporation fractionation is negligible; 2) a 35-cm-thick soil column subject to evaporation where evaporation fractionation process is dominant. The accuracy of the parameterization obtained by the PSO algorithm is assessed based on its ability to reproduce measured water fluxes and isotope transport data. The parameters estimated while considering (or not) evaporation fractionation are then used to calculate travel times and evaporation.

## **2 Materials and Methods**

Two experimental datasets are considered in this study. The first dataset is collected using a field lysimeter (150-cm-thick layered soil profile) located in Austria under humid climate conditions (Stumpp et al., 2012) (Section 2.1.1). The second dataset is collected using a 35-cm-thick soil column (in France) subject to evaporation to mimic arid climate conditions (Braud et al., 2009a) (Section 2.1.2). Numerical simulations of water flow and isotope transport (with and without evaporation fractionation) are implemented in HYDRUS-1D. The modeling setup is briefly described in Section 2.2 and Method S1 in the Supplementary Material. The sensitivity analysis based on the Sobol' and Morris methods is performed to evaluate the interactions between soil hydraulic and solute transport parameters and the impact of multiple measured data types (Section 2.3, Method S2, and Results S1~S2). The accuracy of the parameterization obtained by the PSO algorithm is assessed based on its ability to reproduce the observed data (Sections 2.4, 3.1.1, and 3.2.1). The parameters estimated while considering or not considering evaporation fractionation are then used to calculate travel times and evaporation and quantify the impact of their different estimates (Sections 2.5, 2.6, 3.1.2, and 3.2.2). The effects of varying climate conditions and estimation methods are then compared and illuminated (Section 4).

The schematic outline of the different methods used is shown in Fig. 1. The description of relevant symbols and acronyms is given in the Appendix.

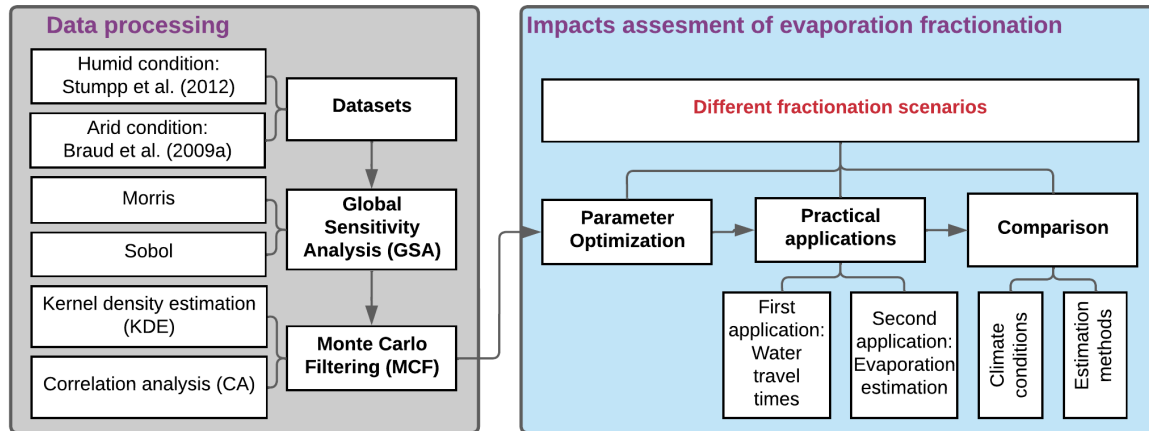


Figure 1. Schematic outline of methods used.

## 2.1 Site description and data availability

### 2.1.1 Stumpp et al. (2012) dataset

The first dataset is taken from the lysimeter 3 of Stumpp et al. (2012) (available at <https://www.pc-progress.com/en/Default.aspx?h1d-lib-isotope>). The field experiment was conducted in a humid region located at the research area of the HBLFA (Höhere Bundeslehr- und Forschungsanstalt für Landwirtschaft) Raumberg-Gumpenstein, in Gumpenstein, Austria. This area has a mean annual temperature of 6.9 °C and average annual precipitation ( $P$ ) of 1035 mm. The annual potential evapotranspiration ( $ET_0$ ) (for grass reference) during the experiment period (May 2002 to February 2007) calculated by the Penman-Monteith equation is about 557 mm, and the corresponding aridity index ( $P/ET_0$ ) is about 1.86, corresponding to a humid climate class (Liang, 1982). The cylindrical lysimeter (with a depth of 150 cm and a surface area of 10000 cm<sup>2</sup>) was embedded in a rainfed agricultural field (Cambisol) planted with winter rye and fertilized with liquid cattle slurry.

The observation period was from May 2002 to February 2007 (1736 days). Table S1 shows the summary of the observed data. The temporal distribution of  $P$ ,  $ET_0$ , soil surface temperature ( $T_s$ ), air relative humidity ( $RH$ ), and leaf area index ( $LAI$ ) during the simulation period are shown in Fig. 2. More details

about data acquisition, including meteorological parameters and root water uptake information, can be found in Stumpp et al. (2012).

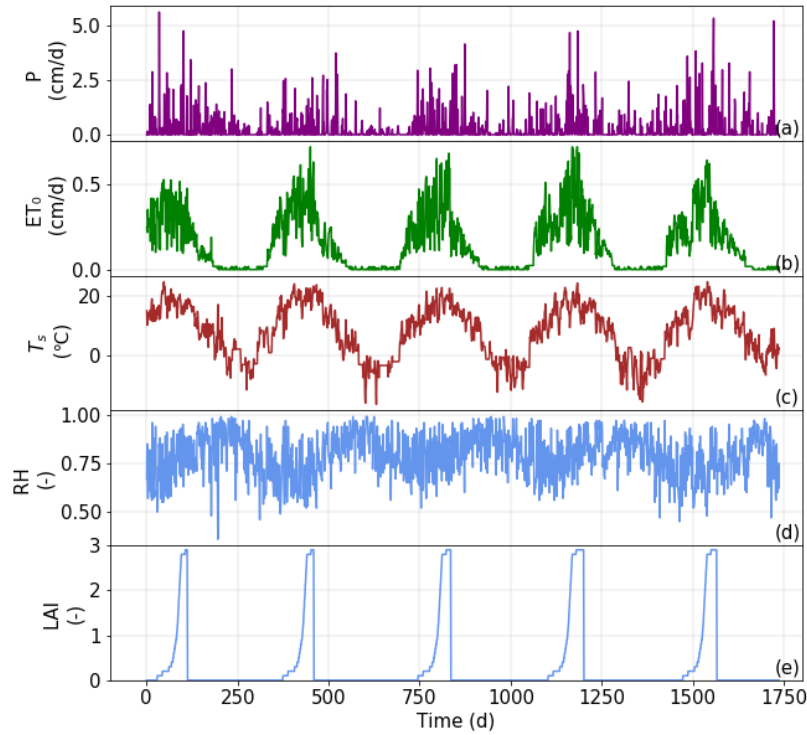


Figure 2. The temporal distribution of precipitation ( $P$ ) (a), potential evapotranspiration ( $ET_0$ ) (b), soil surface temperature ( $T_s$ ) (c), air relative humidity ( $RH$ ) (d), and leaf area index ( $LAI$ ) (e) during the simulation period for the Stumpp et al. (2012) dataset (adapted from Stumpp et al., 2012).

### 2.1.2 Braud et al. (2009a) dataset

Braud et al. (2009a) designed a RUBIC IV experiment that started on April 11, 2005, corresponding to Day of the Year (DoY) 101, and lasted 338 days. The experiment consisted of 6 columns, 12 cm in diameter and 35 cm in height. The soil columns were filled with a silt loam collected at the field station of Lusignan, France, and wetted using demineralized water of the known isotopic composition. The bottom was closed by clay marbles. The soil was initially saturated and subject to evaporation only. Dry air was simultaneously injected over all six columns. The isotopic composition of the air changed due to water vapor released by evaporation from soil columns. The air was finally trapped in a cryoscopic device, which



175 allowed the determination of evaporation fluxes from bare soil columns and the corresponding isotopic  
176 composition of the water vapor under non-steady-state conditions. More details about the experimental setup  
177 can be found in Figs. 1~2 of Braud et al. (2009a). The data collected in Column 2, ending at DoY 264, were  
178 analyzed in this study.

179         Thirteen variables were measured continuously at a frequency of about 15 minutes to assess the  
180 water balance of the soil column. These variables included the room temperature, the atmospheric pressure,  
181 the absolute pressure of the dry air before it entered the soil column, air mass flow for the humidity control  
182 above the soil column, the mass of the soil column, air temperature and humidity at the outlet of the soil  
183 column, the temperatures of the cryoscopic trapping downstream and upstream of the columns, and the air  
184 temperature and residual air humidity at the outlets of two cold traps. The vapor was trapped twice a day  
185 during the first three months and only once a day after that once evaporation decreased. Soil column 2 was  
186 dismantled on September 21, 2005 (DoY 264) to sample liquid water and measure the gravimetric soil water  
187 content. More details about data acquisition can be found in Braud et al. (2009a). The temporal distributions  
188 of the evaporation flux ( $E$ ), the isotopic composition of the evaporation flux ( $\delta_E$ ), outlet air temperature  
189 ( $T_{air}$ ), and outlet air relative humidity ( $RH$ ) during the simulation period are shown in Fig. 3.

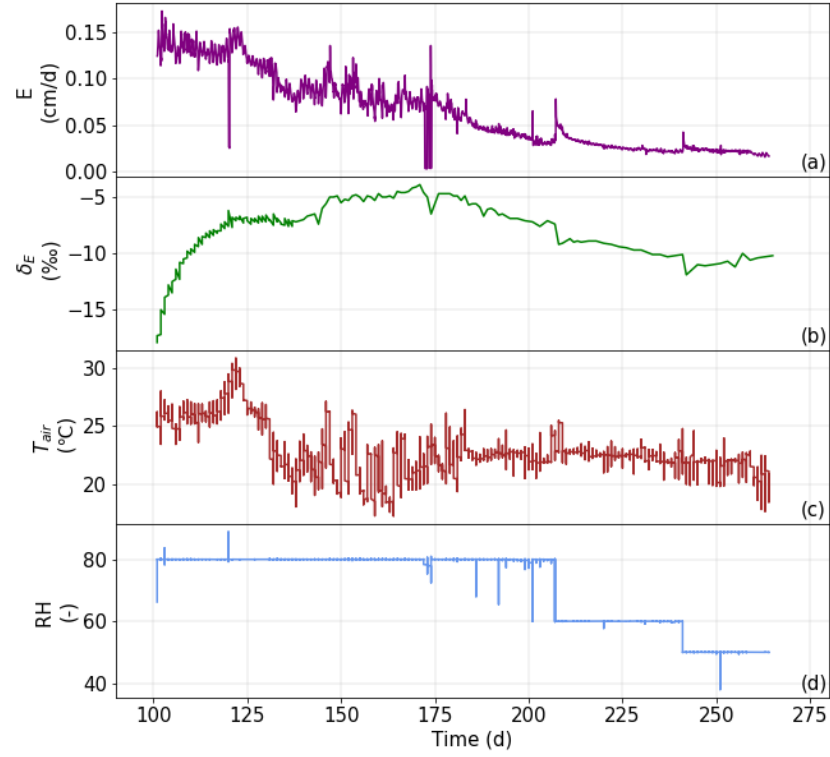


Figure 3. Time series of the evaporation flux ( $E$ ) (a) isotopic composition of the evaporation flux ( $\delta_E$ ) (b), outlet air temperature ( $T_{air}$ ) (c), outlet air relative humidity ( $RH$ ) (d), during the simulation period for the Braud et al. (2009a) dataset (adapted from Braud et al., 2009a).

## 2.2 Model setup

The HYDRUS-1D model modified by Zhou et al. (2021) to simulate the transport of soil water isotopes while considering evaporation fractionation was used in this study. A brief summary of the model setup, including the governing equations (without and with vapor flow for the Stumpp et al. (2012) and Braud et al. (2009a) datasets, respectively), boundary conditions (BCs), and model inputs is shown in Figs. 4~5. More details can be found in Zhou et al. (2021).

### 2.2.1 Stumpp et al. (2012) dataset

The soil profile was 150 cm deep and was discretized into 151 nodes. It consisted of three different soil horizons (0 ~ 29 cm; 30 ~ 89 cm; 90 ~ 150 cm). The initial pressure head profile was assumed to be at hydrostatic equilibrium with the pressure head  $h = -150$  cm at the soil surface. The weighted average  $\delta^{18}\text{O}$  of precipitation (-9.5‰) and estimated temperature (20 °C) were used as initial conditions.

The atmospheric (with a surface layer) and seepage face boundary conditions (BC) were used for water flow at the upper and lower boundaries, respectively. The temperature BC was used for heat transport at both boundaries. In this humid condition example, evaporation fractionation was limited to the soil surface due to the lack of the vapor phase within the soil. The solute flux and zero concentration gradient BCs were used for isotope transport at the upper and lower boundaries, respectively. The isotope flux associated with evaporation was calculated either assuming no fractionation or using the Craig-Gordon or Gonfiantini fractionation models (hereafter referred to as Non\_Frac, CG\_Frac, and Gon\_Frac, respectively). The Non\_Frac scenario calculated the isotope flux of evaporation by assuming that the isotopic composition of the evaporation flux was the same as that of surface soil water. The isotopic composition of the atmospheric water vapor ( $\delta_A$ ) in the CG\_Frac scenario was estimated based on its equilibrium relationship with the isotopic composition of rainfall (Skrzypek et al., 2015). The Gon\_Frac scenario was simplified (without the need for the isotopic composition of the atmospheric water vapor) to consider fractionation (Zhou et al., 2021). A detailed description of the CG and Gonfiantini models can be found in Method S1. For simplification, only equilibrium fractionation was considered at the soil surface since kinetic fractionation could be neglected in this example (Zhou et al., 2021). In other words, the kinetic fractionation coefficient ( $n_k$ ) in Eq. (11) of Zhou et al. (2021) was set to 0, and thus the kinetic fractionation factor at the soil surface ( $\alpha_i^k$ ) in the CG\_Frac and Gon\_Frac scenarios (Eqs. S2, S3) was equal to 1.

Conceptual model	Equations and BCs	Inputs	Abbreviations
<p>humid condition example</p> <p>Note: evaporation fractionation is limited to the soil surface (due to the lack of the vapor phase within soil). For simplicity, only equilibrium fractionation is considered.</p>	<p>➤ <b>Upper BCs:</b></p> <ul style="list-style-type: none"> <li>• <b>W:</b> Atmospheric BC</li> <li>• <b>H:</b> Temperature BC</li> <li>• <b>I:</b> Non_Frac, Gon_Frac, CG_Frac</li> </ul> <p>➤ <b>The governing equations:</b></p> <ul style="list-style-type: none"> <li>• <b>W</b> <math>\frac{\partial \theta_i}{\partial t} = \frac{\partial}{\partial z} \left[ K_{Lh} \left( \frac{\partial h}{\partial z} + \cos \omega \right) \right] - S</math></li> <li>• <b>H</b> <math>\frac{\partial C_p(\theta_i)T}{\partial t} = \frac{\partial}{\partial z} \left[ \lambda(\theta_i) \frac{\partial T}{\partial z} \right] - C_w \frac{\partial q_i T}{\partial z} - C_w S T</math></li> <li>• <b>I</b> <math>\frac{\partial \theta_i C_i^l}{\partial t} = \frac{\partial}{\partial z} (D_i^l \frac{\partial C_i^l}{\partial z}) - \frac{\partial (q_i C_i^l)}{\partial z} - S C_i^l</math></li> </ul> <p>➤ <b>Lower BCs:</b></p> <ul style="list-style-type: none"> <li>• <b>W:</b> Seepage face BC</li> <li>• <b>H:</b> Temperature BC</li> <li>• <b>I:</b> Zero concentration gradient</li> </ul>	<p>➤ <b>Upper BCs:</b></p> <ul style="list-style-type: none"> <li>• <b>W:</b> <math>P, ET_0, LAI</math>, crop growth and RWU parameters.</li> <li>• <b>H:</b> <math>T_s</math></li> <li>• <b>I:</b> <math>\delta_P, RH, \delta_A</math></li> </ul> <p>• <b>W:</b> VG-M model: <math>\theta_r, \theta_s, n, \alpha, K_s</math> (optimized).</p> <p>• <b>H:</b> Chung-Horton model: parameters from Stumpp et al. (2012).</p> <p>• <b>I:</b> <math>D_i^{l0}</math> (calculated), <math>\lambda</math> (optimized).</p> <p>➤ <b>Lower BCs:</b></p> <ul style="list-style-type: none"> <li>• <b>W:</b> None</li> <li>• <b>H:</b> <math>T_b</math></li> <li>• <b>I:</b> None</li> </ul>	<p><math>C_p(\theta_i), C_w</math>: volumetric heat capacities of the porous medium, and the liquid phase, respectively</p> <p><math>C_i^l</math>: isotope concentrations of soil water</p> <p><math>D_i^l</math>: effective dispersion coefficient of the isotope <math>i</math> in soil water</p> <p><math>D_i^{l0}</math>: molecular diffusion coefficient of isotope <math>i</math> in free water</p> <p><math>E</math>: actual evaporation</p> <p><math>ET_0</math>: potential evapotranspiration</p> <p><math>h</math>: water pressure head</p> <p><math>K_{Lh}</math>: isothermal hydraulic conductivity of the liquid phase</p> <p><math>K_s</math>: saturated hydraulic conductivity</p> <p><math>LAI</math>: leaf area index</p> <p><math>n, \alpha</math>: shape parameters of the VG model</p> <p><math>P</math>: precipitation rate</p> <p><math>Q</math>: drainage or discharge</p> <p><math>q_i</math>: liquid water flux</p> <p><math>RH</math>: air relative humidity</p> <p><math>S</math>: sink term</p> <p><math>t</math>: time</p> <p><math>T_s</math>: soil bottom temperature</p> <p><math>T_s</math>: soil surface temperature</p> <p><math>z</math>: spatial coordinate (positive upward)</p> <p><math>\omega</math>: angle between the flow direction and the vertical axis</p> <p><math>\delta_A</math>: isotopic composition of the atmospheric water vapor</p> <p><math>\delta_P</math>: isotopic composition of precipitation</p> <p><math>\theta_i</math>: liquid volumetric water content</p> <p><math>\theta_r</math>: residual water content</p> <p><math>\theta_s</math>: saturated water content</p> <p><math>\lambda</math>: longitudinal dispersivity</p> <p><math>\lambda(\theta_i)</math>: coefficient of the apparent thermal conductivity of the soil</p>

224

225

Figure 4. Model setup for the Stumpp et al. (2012) dataset. Note that "W," "H," and "I" represent water

226

flow, heat transport, and isotope transport, respectively.

227

### 228 2.2.2 Braud et al. (2009a) dataset

229

The simulated soil profile was 35 cm deep and was discretized into 132 nodes following Braud et al. (2009a). The soil column was initially almost fully saturated, with the measured initial pressure head increased linearly from  $-1$  cm at the soil surface to 35 cm at the soil profile bottom. The observed initial soil temperature and  $\delta^{18}\text{O}$  were  $24.25^\circ\text{C}$  and  $-6.34\%$ , respectively.

233

The temperature BC was used for heat transport at both surface and bottom boundaries, using temperatures measured at 2.5 and 24 cm depths, respectively. The atmospheric and zero flux BCs were used for water flow at the upper and lower boundaries, respectively. The measured evaporation flux,  $E$  was used as the upper BC for water flow. In this arid condition example, evaporation fractionation occurred both at the soil surface and within the soil due to the existence of the vapor phase. The stagnant air layer BC (which had been modified to account for evaporation fractionation) and zero flux BC were used for isotope transport

238

at the upper and lower boundaries, respectively. The surface isotope flux associated with evaporation was calculated either assuming no fractionation, using the Craig-Gordon or Gonfiantini fractionation models, or using the measured values (hereafter referred to as Non\_Frac, CG\_Frac, Gon\_Frac, and Meas\_Frac, respectively). The Non\_Frac scenario calculated the isotope flux of evaporation by assuming that its isotopic composition was the same as that of surface soil water (i.e., no fractionation at the soil surface), and equilibrium and kinetic fractionation factors within the soil ( $\alpha^+$ ,  $\alpha_i^D$ ) were equal to 1 (i.e., no fractionation within the soil). The theory of CG\_Frac and Gon\_Frac scenarios was explained in Method S1. For simplification, the kinetic fractionation coefficient  $n_k$  in Eq. (11) of Zhou et al. (2021) was set to 1, and thus the kinetic fractionation factor at the soil surface ( $\alpha_i^k$ ) in the CG\_Frac and Gon\_Frac scenarios (Eqs. S2, S3) was equal to 1.0324. The measured isotopic composition of the outlet water vapor,  $\delta_E$ , was used in the Meas\_Frac scenario to calculate the surface isotope flux  $E_i$  corresponding to the evaporation flux  $E$ . More details about how upper boundary fluxes were calculated can be found in Braud et al. (2009a).

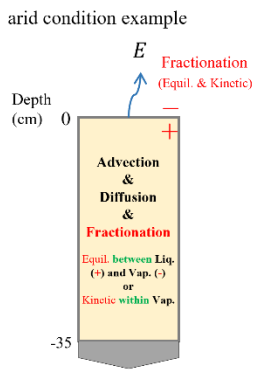
Conceptual model	Equations and BCs	Inputs	Abbreviations
<p>arid condition example</p>  <p>Note: evaporation fractionation happens both at the soil surface and within soil (due to the existence of the vapor phase). Both equilibrium and kinetic fractionation are considered.</p>	<p>➤ <b>Upper BCs:</b></p> <ul style="list-style-type: none"> <li>• <b>W:</b> Atmospheric BC</li> <li>• <b>H:</b> Temperature BC</li> <li>• <b>I:</b> Non_Frac, Gon_Frac, CG_Frac, Meas_Frac</li> </ul> <p>➤ <b>Lower BCs:</b></p> <ul style="list-style-type: none"> <li>• Zero flux BC</li> <li>• Temperature BC</li> <li>• Concentration flux BC</li> </ul> <p>➤ <b>The governing equations:</b></p> <ul style="list-style-type: none"> <li>• <b>W</b>  <math display="block">\frac{\partial \theta_f(h)}{\partial t} = \frac{\partial}{\partial z} \left[ K_{Lh} \left( \frac{\partial h}{\partial z} + \cos \omega \right) + K_{LT} \frac{\partial T}{\partial z} + K_{vh} \frac{\partial h}{\partial z} + K_{vt} \frac{\partial T}{\partial z} \right]</math> </li> <li>• <b>H</b>  <math display="block">C_p(\theta_i) \frac{\partial T}{\partial t} + L_0 \frac{\partial \theta_i}{\partial t} = \frac{\partial}{\partial z} \left( \lambda(\theta_i) \frac{\partial T}{\partial z} \right) - C_w q_i \frac{\partial T}{\partial z} - C_v \frac{\partial q_v T}{\partial z} - L_0 \frac{\partial q_v}{\partial z}</math> </li> <li>• <b>I</b>  <math display="block">\frac{\partial [\theta_i C_i^l]}{\partial t} = \frac{\partial}{\partial z} \left[ D_i^{lv*} \frac{\partial C_i^l}{\partial z} - Q_i^{lv*} C_i^l \right]</math> <math display="block">\theta_i = [\theta_l + (n_{soil} - \theta_l) \beta_i^l]</math> <math display="block">Q_i^{lv*} = (q_l + \beta_i^l q_v - D_i^{lv*} \frac{\partial \beta_i^l}{\partial z})</math> <math display="block">D_i^{lv*} = D_i^{l*} + D_i^{v*} \beta_i^l</math> <math display="block">C_i^v = \beta_i^l C_i^l = \alpha_i^* \frac{\rho_v}{\rho_w} C_i^l</math> </li> </ul>	<p>➤ <b>Upper BCs:</b></p> <ul style="list-style-type: none"> <li>• <b>W:</b> <math>E</math></li> <li>• <b>H:</b> <math>T_s</math></li> <li>• <b>I:</b> <math>RH, \delta_A, \delta_E</math></li> </ul> <p>• <b>W:</b> VG-M model: <math>\theta_r, \theta_s, n, \alpha, K_s</math> (optimized).</p> <p>• <b>H:</b> Chung-Horton model: parameters from Braud et al. (2009a).</p> <p>• <b>I:</b> <math>D_i^{l0}, D_i^l</math> (calculated), <math>\lambda</math> (optimized).</p> <p>➤ <b>Lower BCs:</b></p> <ul style="list-style-type: none"> <li>• <b>W:</b> 0</li> <li>• <b>H:</b> <math>T_b</math></li> <li>• <b>I:</b> None</li> </ul>	<p><math>C_i^l</math>: isotope concentrations in soil water (vapor), respectively</p> <p><math>C_v</math>: volumetric heat capacities of the vapor phase, respectively</p> <p><math>D_i^{lv*}</math>: effective dispersion coefficients of the isotope <math>i</math> in soil water vapor</p> <p><math>D_i^l</math>: molecular diffusion coefficient of isotope <math>i</math> in free air, respectively</p> <p><math>K_{LT}</math>: thermal hydraulic conductivity of the liquid phase</p> <p><math>K_{vh}</math>: isothermal vapor hydraulic conductivity</p> <p><math>K_{vt}</math>: thermal vapor hydraulic conductivity</p> <p><math>L_0</math>: volumetric latent heat of vaporization of liquid water</p> <p><math>n_{soil}</math>: soil porosity</p> <p><math>q_v</math>: vapor flux</p> <p><math>\beta_i^l</math>: ratio of the isotope concentration in the vapor phase and the isotope concentration in the liquid phase</p> <p><math>\delta_E</math>: isotopic composition of evaporation flux</p> <p><math>\theta_T</math>: total volumetric water content, being the sum (<math>\theta_T = \theta_l + \theta_v</math>)</p>

Figure 5. Model setup for the Braud et al. (2009a) dataset. Note that "W," "H," and "I" represent water flow, heat transport, and isotope transport, respectively.

## 2.3 Global sensitivity analysis

Five soil hydraulic parameters (i.e.,  $\theta_r$ ,  $\theta_s$ ,  $n$ ,  $\alpha$ , and  $K_s$ ) need to be optimized for each layer of the soil profile to simulate water flow using the HYDRUS-1D model. The residual water content  $\theta_r$  was set to zero to reduce the number of fitting parameters. To simulate isotope transport in the soil, the longitudinal dispersivity  $\lambda$  also needs to be optimized. Since only the isotopic composition of the lysimeter discharge was measured in the Stumpp et al. (2012) dataset, the dispersivity of three individual soil layers cannot be estimated. Therefore, only one longitudinal dispersivity for the entire lysimeter was estimated. Therefore, the total number of parameters  $p$  was 13 and 5 for the Stumpp et al. (2012) and Braud et al. (2009a) datasets, respectively. The global sensitivity analysis (GSA) using both Morris and Sobol' methods was conducted in this study to determine the most influential parameters and their interactions. The detailed description of these two methods is shown in Method S2 in the Supplementary Material.

The sensitivity analysis was conducted using Python's Sensitivity Analysis Library (SALib) (Herman and Usher, 2017). The script produces the input parameter space, overwrites the input parameters file, and runs the executable module of HYDRUS-1D. For each simulation of the Stumpp et al. (2012) dataset, five Kling-Gupta efficiency (KGE) indices for different evaluation indicators were calculated, including for the time series of the bottom water flux (KGE\_bf), the soil water content at different depths (KGE\_wc), the bottom water isotopic composition (KGE\_wi), the water retention curves (KGE\_rc), and the average of the four KGE values (KGE\_avg). For each simulation of the Braud et al. (2009a) dataset, three Kling-Gupta efficiency (KGE) indices for different evaluation indicators were calculated, including the final soil water content profile (KGE\_wc), the final water isotopic composition profile (KGE\_wi), and the average of the two KGE values (KGE\_avg). The KGE index compares the correlation coefficient ( $r$ ), the ratio of mean values ( $\beta$ ), and the ratio of variances ( $\gamma$ ) between simulated and observed data. The value of the KGE index is always smaller or equal to 1. The higher the KGE value, the better fit between the simulated and observed values. The positive and negative KGE values are often considered "good" and "bad" solutions (Knoben et al., 2019).

$$KGE = 1 - [(1 - r)^2 + (1 - \beta)^2 + (1 - \gamma)^2]^{0.5} \quad (1)$$

If a HYDRUS-1D run was not finished within a prescribed time (i.e., 30 s and 60 s for the Stumpp et al. (2012) and Braud et al. (2009a) datasets, respectively) or the length of the modeled hydrograph was shorter than the total simulation period (1736 and 163 days for the Stumpp et al. (2012) and Braud et al. (2009a) datasets, respectively), it was considered non-convergent. The run was then terminated, and a large negative value ( $-1E+7$ ) was prescribed to the objective function.

Non-convergent runs in GSA are a frequent problem when using nonlinear environmental/hydrological models, and there are no clear indications on how to handle these "unfeasible" points (Razavi et al., 2021). Removing or skipping them alters the sampling trajectory and can result in biased conclusions, especially if non-convergent runs lie in informative regions of the parameter space. Recently, Sheikholeslami et al. (2019) compared strategies such as median substitution, single nearest-neighbor, or response surface modeling (Brunetti et al., 2017) to fill in for model crashes. Their results show that interpolating non-convergent runs with a radial basis function trained in the vicinity of that point leads to reliable results and outperforms other strategies. We implemented a similar approach in the present work but with important differences. In particular:

1. For each non-convergent point, we calculated its Euclidean distance from all other convergent points in the GSA sample.
2. Convergent points were ordered in ascending order (i.e., from the closest to the farthest).
3. The 100 closest convergent points were used to train a response surface surrogate based on the Kriging Partial Least Squares method (KPLS) (Bouhlef et al., 2016), which outperforms traditional kriging on high-dimensional problems.
4. The trained KPLS surrogate was finally used to interpolate non-convergent runs in the original GSA sample.

The use of multiple localized surrogates allowed for better reconstruction of the topological features of the response surface in the vicinity of the non-convergent points.

In this study, the global sensitivity analysis was combined with the Monte Carlo filtering to identify reduced ranges of parameters with good solutions for subsequent parameter optimization. Potential solutions were filtered into good solutions with  $KGE > 0.0$  and bad solutions with  $KGE \leq 0.0$ . Kernel density estimation (KDE) plots were then used to identify areas with high-density good solutions, while the correlation analysis was conducted to determine interactions between parameters and may help reduce the input factor space. More details can be found in Brunetti et al. (2016). This type of procedure shares multiple similarities with the Generalized Likelihood Uncertainty Estimation (GLUE) proposed by Beven et al. (2001). The joint use of the GSA sample with the GLUE approach [i.e., GSA-GLUE (Ratto et al., 2001)] allows for obtaining a rough assessment of the parameters uncertainty and successful estimates of soil hydraulic parameters (e.g., Brunetti et al., 2018).

## **2.4 Parameter optimization**

The Particle Swarm Optimization (PSO) algorithm was used in this study for parameter optimization. In the PSO, a swarm of candidate solutions is moved around in the search space according to a few equations. The movement of the particles is guided by the optimal position of themselves and the whole swarm. Once improved positions are discovered, they are used to guide the swarm's movement. This process is repeated until the global optimal position that all particles tend to follow is found (Shi and Eberhart, 1998).

The PSO parameters (cognitive parameter  $c_1 = -0.267$ ; social parameter  $c_2 = 3.395$ ; inertia-weight  $w = -0.444$ ) from Brunetti et al. (2016) were used in this study. The number of particle swarm and iterations are 40 and 200, respectively.

The PySwarm Library in Python was used for the PSO. The process was similar to the GSA, except that reduced ranges of parameters were used. In this way, the number of potential local minima is reduced, and the convergence improves. Only the set of parameters leading to the maximum  $KGE_{avg}$  (i.e., minimum  $1 - KGE_{avg}$  as the objective function) was retained as optimized parameters.



## 2.5 First practical application: Calculation of drainage and RWU travel times

### 2.5.1 The peak displacement (isotope-transport-based) method

The peak displacement method estimates travel times from the time lag between signals in the measured input (rainfall isotopic composition) and output (drainage isotopic composition) isotope time series. In the Stumpp et al. (2012) dataset, a pronounced correspondence was observed between the depleted precipitation peak in the winter (November 18, 2005, to April 14, 2006) and the lysimeter discharge. The mean drainage travel time  $t_o^*$  [T], accounting for dispersion effects, can be calculated by the mean peak isotopic composition lag time  $t_m^*$  [T] using Eq. 2:

$$t_o^* = \frac{t_m^*}{\sqrt{1 + (3\frac{\lambda}{L})^2} - 3\frac{\lambda}{L}} \quad (2)$$

where  $L$  is the lysimeter length [L]. More details can be found in Stumpp et al. (2012). In this study,  $t_m^*$  from Stumpp et al. (2012) and dispersivities  $\lambda$  optimized using HYDRUS-1D assuming different fractionation scenarios were used.

### 2.5.2 The particle tracking (water-flow-based) method

The particle tracking algorithm is based on the water mass balance calculation. The initial position of the particles is defined using the initial water content distribution. Depending on the precipitation/irrigation inputs, the particles may be released at the soil surface and leave at the soil profile bottom. In this study, the input parameters  $w_{Stand}$  (the initial distribution) and  $w_{Prec}$  (the upper BC distribution) for the particle tracking algorithm were set to 10 cm and a negative number (which triggers the option of releasing particles with each rain event), respectively. More details about the particle tracking algorithm can be found in Šimůnek (1991) or Zhou et al. (2021).

When knowing the positions of the particles at different times, the residence time ( $RT$ ) and locations of water from all precipitation/irrigation events can be obtained, i.e., the residence time distribution ( $RTD$ ).

Note that the particle travel time ( $TT$ ) is the sum of the particle age (i.e., residence time) and life expectancy (i.e., time to reach the destination). The former is the time elapsed since the particle release, while the latter is the remaining time before the particle reaches the outlet (Benettin et al., 2015). Therefore, when the particles leave the lysimeter bottom or as root water uptake (RWU), their residence times can be called drainage or RWU travel times, respectively. The particle tracking module additionally assesses RWU between two neighboring particles as a function of time. When particles are released for each precipitation event, we can precisely evaluate the contribution of each precipitation event to RWU at different times. We can then infer the temporal origin of RWU by synthesizing this information. Different fractionation scenarios with the soil hydraulic parameters optimized using HYDRUS-1D were used to run the particle tracking module to calculate drainage and RWU travel times.

## **2.6 Second practical application: Calculation of evaporation flux**

### **2.6.1 The water-flow-based method**

Braud et al. (2009a) calculated evaporation using three methods. The first method determines the evaporation rate by continuously measuring the vapor flux and humidity at the outlet of the soil column. The second method obtains the evaporation rate by repeatedly weighing the soil column. Finally, the third method determines the evaporation rate by weighting the mass of the frozen water trapped at the outlet of the soil column. These three methods are hereafter referred to as direct measurement, column weighting, and trapped volume, respectively. This study presents these results also as the reference for other methods. More details can be found in Braud et al. (2009a). Another water-flow-based method used in this study to calculate water flux components was to analyze the water mass balance simulated in HYDRUS-1D (e.g., Sutanto et al., 2012).

## 2.6.2 The isotope-transport-based method

For an isolated water volume with an initial isotopic composition,  $\delta_0$  (‰) evaporating into the atmosphere, the isotopic composition of the residual liquid water  $\delta_s$  (‰) can be calculated as (Benettin et al., 2018):

$$\delta_s = (\delta_0 - \delta^*)(1 - F_E)^{xm} + \delta^* \quad (3)$$

where  $\delta^*$  (‰) is the limiting isotopic composition that would be approached when water is drying up,  $xm$  is the temporal enrichment slope (–), and  $F_E$  is described below.

Eq. (3) is based on the isotope mass balance equations of Gonfiantini (1986) and the isotopic composition of the evaporation flux estimated by the Craig–Gordon model (Craig and Gordon, 1965). More details about the derivations can be found in Gonfiantini (1986). This equation implies that the isotopic composition of soil water only changes due to evaporation fractionation. The ratio of the evaporation loss to the initial water storage ( $F_E$ ) can be then estimated as (Sprenger et al., 2017):

$$F_E = 1 - \left[ \frac{(\delta_s - \delta^*)}{(\delta_0 - \delta^*)} \right]^{\frac{1}{xm}} \quad (4)$$

The two variables  $\delta^*$  and  $xm$  can be calculated as (Benettin et al., 2018):

$$\delta^* = \frac{(RH \cdot \delta_A + \varepsilon_k + \varepsilon^+ / \alpha^+)}{(RH - 10^{-3}(\varepsilon_k + \varepsilon^+ / \alpha^+))} \quad (5)$$

$$xm = \frac{(RH - 10^{-3}(\varepsilon_k + \varepsilon^+ / \alpha^+))}{(1 - RH + 10^{-3}\varepsilon_k)} \quad (6)$$

where  $\delta_A$  (‰) is the isotopic composition of the atmospheric water vapor,  $RH$  is the air relative humidity,  $\alpha^+$  (–) is the dimensionless equilibrium fractionation factor, while  $\varepsilon^+$  (‰) and  $\varepsilon_k$  (‰) are equilibrium and kinetic fractionation enrichments, respectively. Details about the calculation procedure for these parameters ( $\alpha^+$ ,  $\varepsilon^+$ ,  $\varepsilon_k$ ) can be found in Benettin et al. (2018) or Zhou et al. (2021). The equivalent kinetic fractionation factor within the soil ( $\alpha_i^D$ ) used to calculate  $\varepsilon_k$  was optimized manually to get the best match of  $F_E$  with those from water-flow-based methods in Section 2.6.1.

The fraction of water that evaporated before the end of the Braud et al. (2009a) experiment was calculated in this study. Average measured values of  $RH$ ,  $T_{air}$ ,  $T_s$ , and  $\delta_0$  during the experiment, and the final isotope profile simulated using HYDRUS-1D were used in the above equations.

### 3 Results

#### 3.1 Stumpp et al. (2012) dataset analysis

##### 3.1.1 Parameter optimization and model performance

The global sensitivity analysis and Monte-Carlo filtering results for the Stumpp et al. (2012) dataset are shown in the Results S1 section of the Supplementary material. Overall, soil hydraulic parameters of different layers had comparable impacts on the model outputs. The order of sensitive parameters is: shape parameters of the water retention function, namely  $n$ , and  $\alpha$ , saturated water content  $\theta_s$ , saturated hydraulic conductivity  $K_s$ , and dispersivity  $\lambda$ . The final optimized soil hydraulic and solute transport parameters and corresponding KGEs are shown in Table 1. Considering evaporation fractionation impacted parameter estimation significantly, especially in the optimization of the soil saturated hydraulic conductivity,  $K_s$ , and shape parameter,  $\alpha$ . Overall, the water retention and soil hydraulic conductivity curves (Fig. S8) differed greatly between different fractionation scenarios in the third layer, but were relatively similar in the first and second layers. The water retention curve in the Gon\_Frac scenario best matched the measured one, but did not outperform those from the CG\_Frac and Non\_Frac scenarios, as seen from the KGE\_rc values in Table 1. Compared with the CG\_Frac and Gon\_Frac scenarios, the water retention curve in the Non\_Frac scenario had a steeper decline and a lower saturated water content in the third layer, while it became more gradual with higher saturated water contents in the first and second layers. However, the Non\_Frac scenario always produced higher hydraulic conductivities than the CG\_Frac and Gon\_Frac scenarios (Note that the Non\_Frac scenario also had higher hydraulic conductivities in the third layer because of relatively higher matric potentials).

The fits for different fractionation scenarios are shown in Fig. 6. The isotopic composition of the lysimeter discharge remained the same for different fractionation scenarios during about the first 150 days

and started deviating after this time, but the trends were still similar except for some vertical shifts. Different fractionation scenarios resulted in a similar average fitting performance (KGE\_avg) (within 0.03). The Non\_Frac scenario had the highest KGE\_wi (i.e., for water isotopic composition), followed by the CG\_Frac scenario, while the Gon\_Frac scenario performed the worst. The difference between KGE\_wi indices for different fractionation scenarios was within 0.09.

Table 1. Optimized parameters and Kling-Gupta efficiency (KGE) indices (bf, wc, wi, and avg refer to the bottom flux, water content, water isotopic composition, and average, respectively) for different fractionation scenarios (Non\_Frac, CG\_Frac, and Gon\_Frac) (for the Stumpp et al. (2012) dataset).

Fractionation scenario	$z$	$\theta_r$	$\theta_s$	$\alpha$	$n$	$K_s$	$\lambda$	KGE_bf	KGE_wc	KGE_wi	KGE_rc	KGE_avg
	cm	cm <sup>3</sup> /cm <sup>3</sup>	cm <sup>3</sup> /cm <sup>3</sup>	cm <sup>-1</sup>	-	cm/d	cm					
Non_Frac	0–30	0	0.31	0.010	1.19	83.6						
	31–90	0	0.43	0.293	1.11	1131.71	5.00	0.99	0.47	0.59	0.87	0.73
	91–150	0	0.30	0.009	1.91	85.16						
CG_Frac	0–30	0	0.30	0.020	1.15	220.00						
	31–90	0	0.41	0.300	1.11	287.24	5.00	0.99	0.54	0.58	0.89	0.75
	91–150	0	0.30	0.082	1.10	220.00						
Gon_Frac	0–30	0	0.30	0.026	1.14	220.00						
	31–90	0	0.40	0.298	1.11	191.89	6.02	0.99	0.45	0.50	0.92	0.72
	91–150	0	0.35	0.300	1.12	220.00						

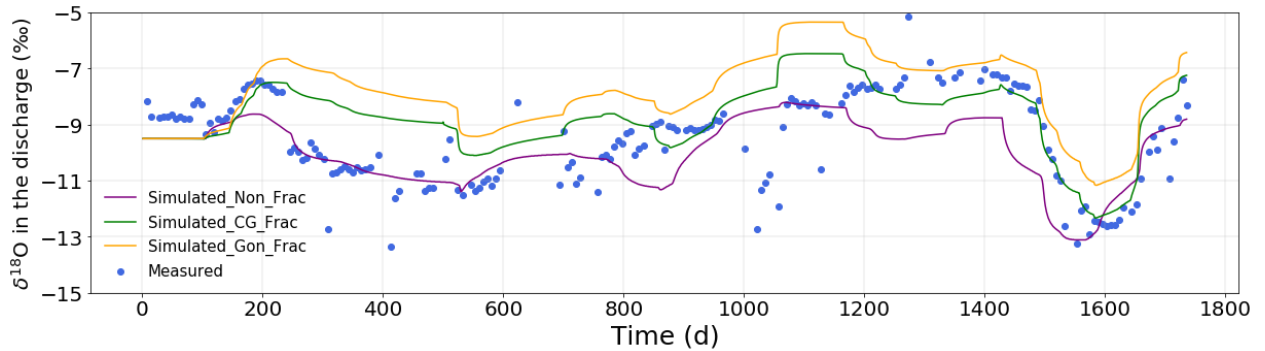


Figure 6. Measured (symbols) and simulated discharge <sup>18</sup>O isotopic compositions for different fractionation scenarios (for the Stumpp et al. (2012) dataset).

### 3.1.2 First practical application: Drainage travel times and RWU temporal origin

The mean travel times (*MTTs*) of drainage (i.e., from the surface to the bottom) estimated by the peak displacement method are shown in Table 2. The *MTTs* were 251.9, 251.9, and 257.1 days for the Non\_Frac, CG\_Frac, and Gon\_Frac scenarios, respectively. The consideration of fractionation using the Gonfiantini model slightly overestimated the travel times compared to the Non\_Frac scenario. However, the difference was not very evident (within 6 days) for different fractionation scenarios.

Table 2. Estimated mean travel times of drainage ( $t_0^*$ ) and mean water fluxes ( $v_0^*$ ) for different fractionation scenarios (Non\_Frac, CG\_Frac, and Gon\_Frac) using different methods (peak displacement and particle tracking).

Method	Fractionation scenario	$t_0^*$ (d)	$v_0^*$ (mm/d)	Ratio of $t_0^*$ compared to $t_0^*$ for Non_Frac
Peak displacement	Non_Frac	251.9	5.95	
	CG_Frac	251.9	5.95	0%
	Gon_Frac	257.1	5.83	2.06%
Particle tracking	Non_Frac	297.5	5.04	
	CG_Frac	356.8	4.20	19.93%
	Gon_Frac	369.9	4.05	24.33%

Fig. S9 shows the spatial-temporal distribution of particles simulated using the soil hydraulic parameters estimated considering different fractionation scenarios. The residence time distribution (*RTD*) of soil water is displayed in Fig. 7. The mean residence time (*MRT* – the mean of *RTs* averaged over the entire simulation duration) increased with soil depth in all scenarios due to a time lag involved in water transfer. The *MRTs* for the Non\_Frac scenario for depths of 30, 70, and 110 cm were 82.1, 138.2, and 203.6 days, respectively. The *MRTs* for the CG\_Frac scenario for 30, 70, and 110 cm depths were 69.9, 170.0, and 258.5 days, respectively. Finally, the *MRTs* for the Gon\_Frac scenario for 30, 70, and 110 cm depths were 80.6, 174.3, and 270.6 days, respectively. In terms of temporal distribution, *RTs* showed five distinct seasonal cycles. Specifically, they had a trough after every rainy season and a peak after every dry season,

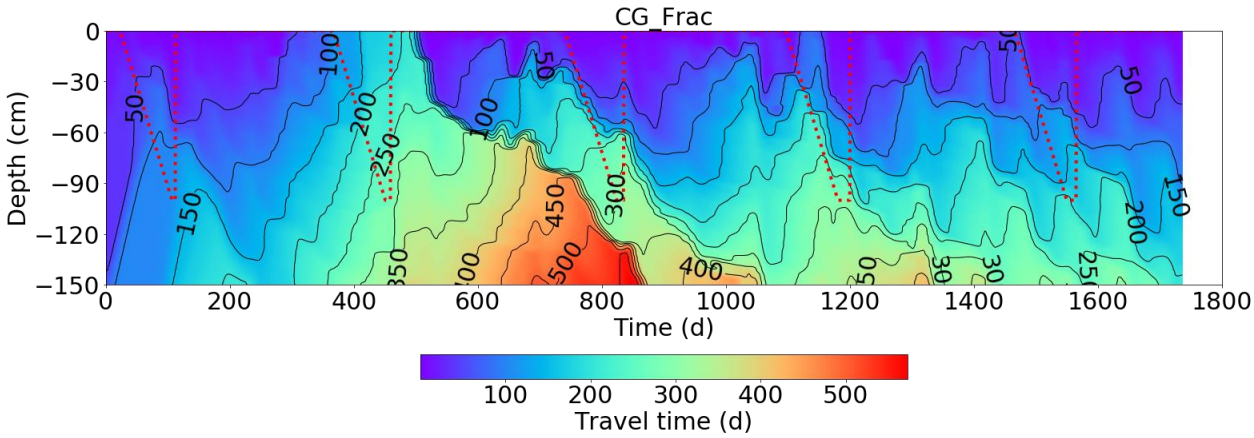
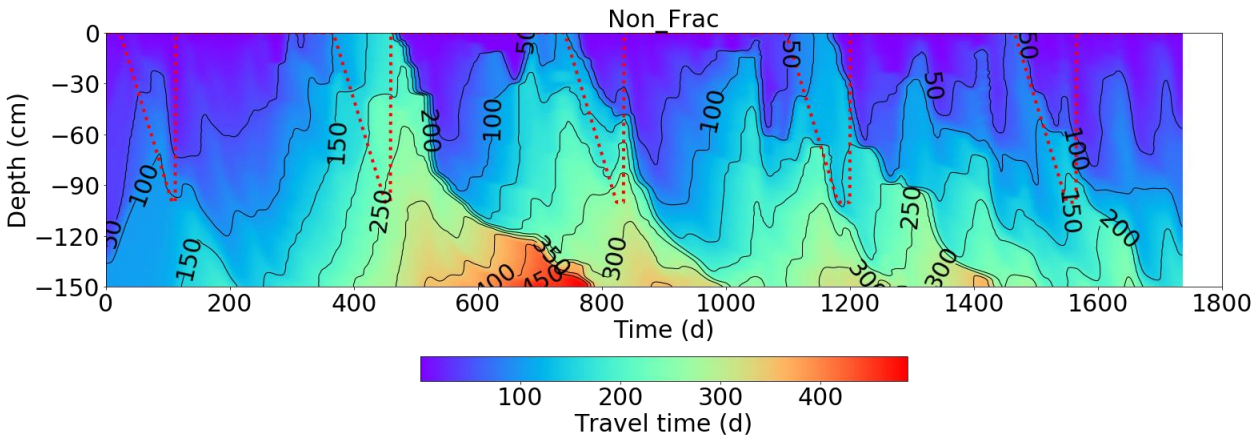
showing a pronounced lag effect. In other words, *RTs* were determined by the trade-off between precipitation input and evapotranspiration removal.

Corresponding travel times of drainage are shown as probability density distribution histograms in Fig. S10 and summarized in Table 2. The means (and standard deviations) of travel times were 297.5 (79.96), 356.8 (104.29), and 369.9 (101.24) days for the Non\_Frac, CG\_Frac, and Gon\_Frac scenarios, respectively. The particle tracking method produced significantly higher travel times (by about 89 days) than the peak displacement method. Similarly, considering fractionation using the CG\_Frac and Gon\_Frac scenarios led to longer travel times (*TTs*) than the Non\_Frac scenario. In addition, the difference was very evident (reached 78 days) for different scenarios.

To further explore and quantify the *RTD* differences when considering different fractionation models, the temporal origin of RWU is plotted in Fig. 8. Fig. 8 shows the monthly transpiration sums in the upper panels and fractional contributions of water of a certain age/origin to these monthly transpiration sums in the lower panels. Note that the amount and temporal distribution of transpiration were similar under different fractionation scenarios (54.95, 53.91, and 54.03 cm for Non\_Frac, CG\_Frac, and Gon\_Frac, respectively). Therefore, only the temporal distribution of transpiration in the Non\_Frac scenario is displayed. As for the age distribution of RWU, for example, in the Non\_Frac scenario, the yellow line in 2002 indicates that about 29% of the water taken up by roots in August was older than May, while the remaining 71% was from May~August of 2002 (5% from June, 16% from July, and 50% from August). More details about how to read the age distribution of RWU can be found in Fig. 5 of Brinkmann et al. (2018).

The maximum water age for RWU for different fractionation scenarios was almost the same, about 300 d in October 2003, 330 d in September 2004, 270 d in November 2005, and 180 d in February 2006, except for 240 d in December 2004 and 180 d in February of 2005 for the Non\_Frac scenario. These results were consistent with water residence times at the maximum rooting depths in Fig. 7. However, different fractionation scenarios had relatively large impacts (up to three months) on the minimum water age for

RWU. The most obvious example was the 2003 growing season (a relatively dry year with less precipitation,  
 as shown in Fig. 2). The minimum water age for RWU in 2003 was within about a month for the Gon\_Frac  
 scenario and 120 d (February) for the Non\_Frac and CG\_Frac scenarios. In addition, the dynamics of  
 fractional monthly contributions to RWU also varied between different scenarios. In general, the water age  
 for RWU was far longer in dry years (2003~2004) than in wet years (2005~2006), suggesting that drought  
 can promote crop uptake of old water. In the same growing season, the water age for RWU was consistently  
 lower in May and June than in July and August, which reflected an increase in the rooting depth.





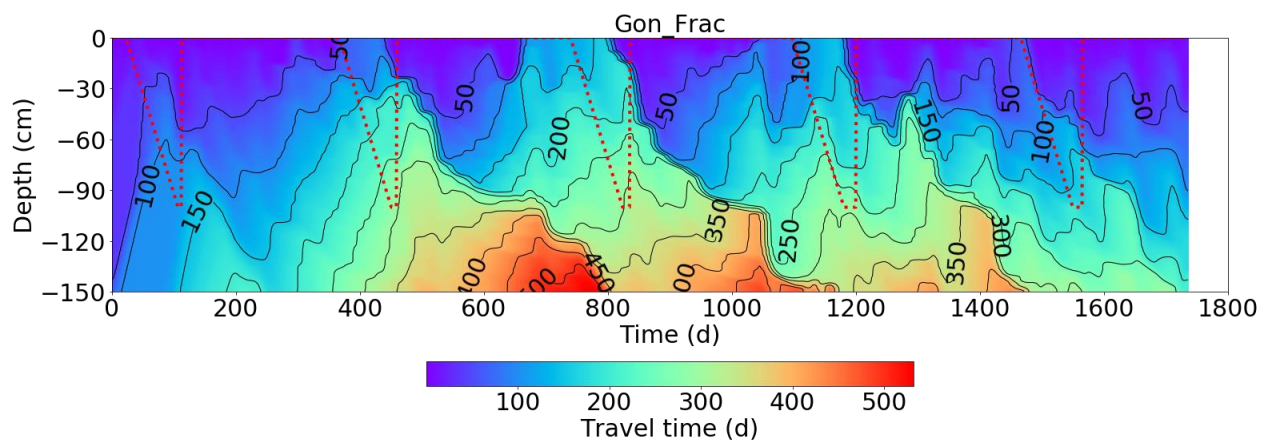
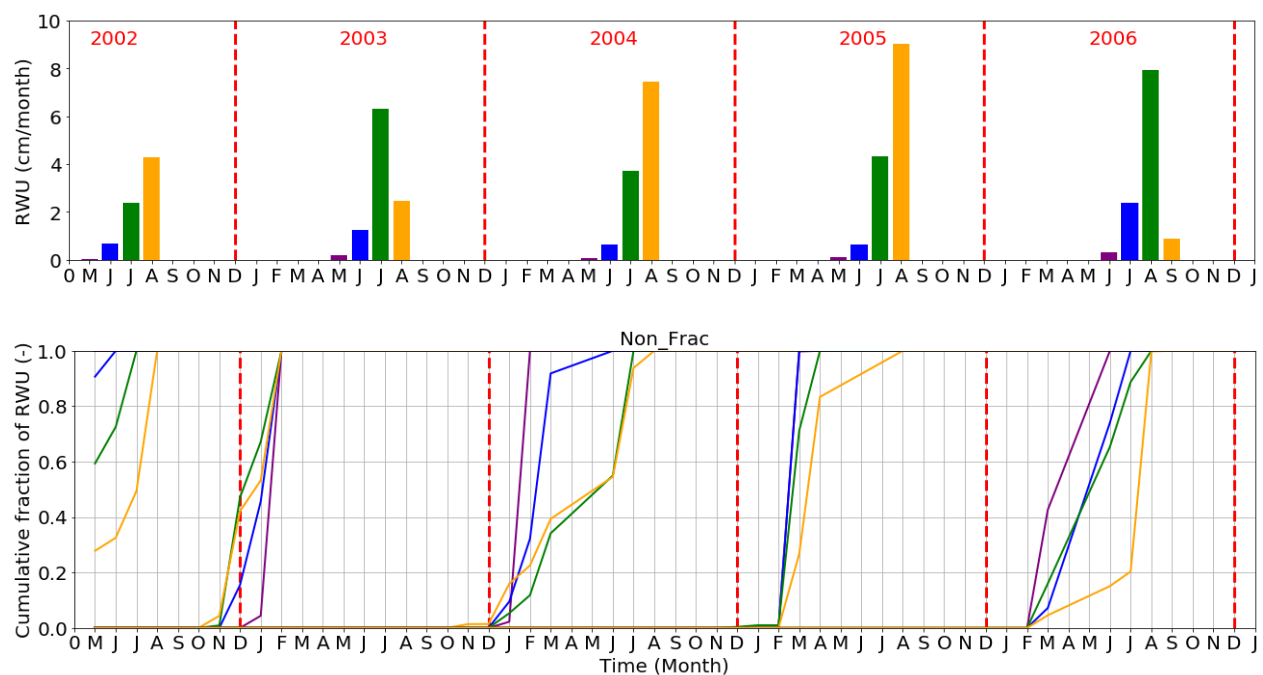


Figure 7. The residence time distributions (*RTDs*) for different fractionation scenarios (Non\_Frac – top, CG\_Frac – middle, and Gon\_Frac – bottom). Note that the dashed red line represents the rooting depth.



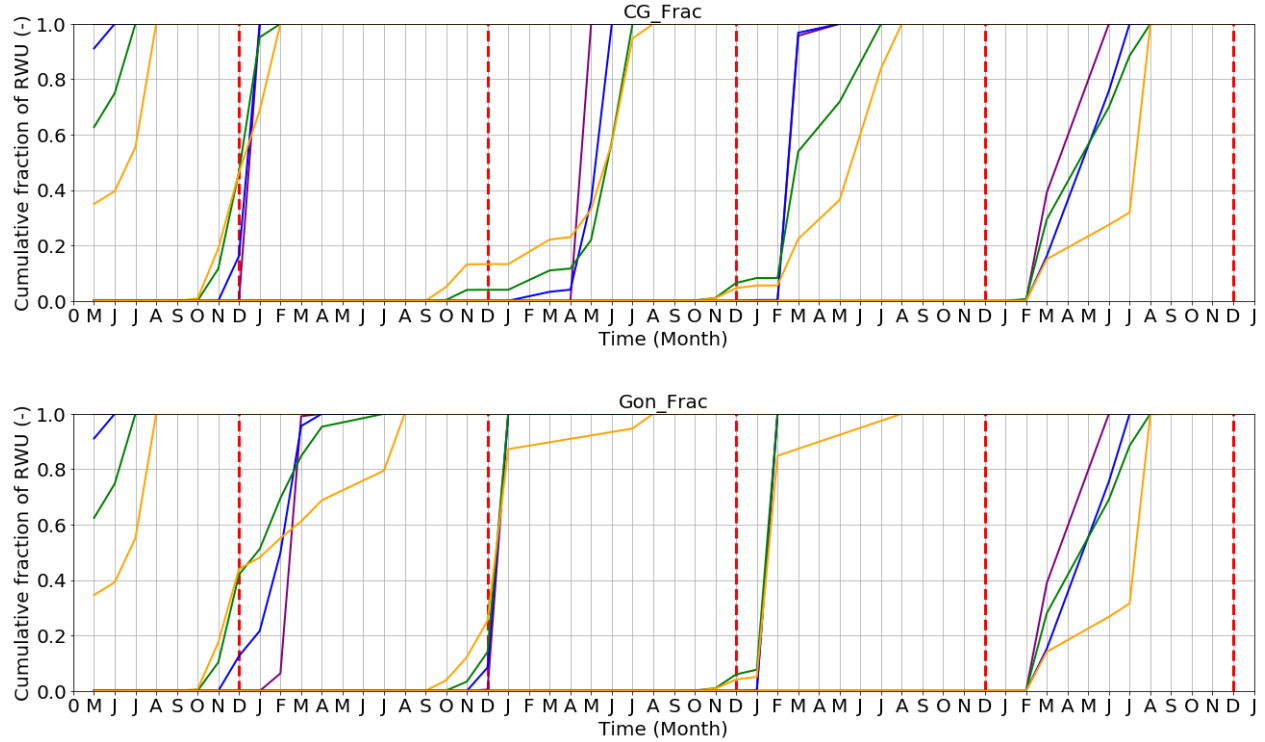


Figure 8. The temporal origin of root water uptake (RWU) for different fractionation scenarios (Non\_Frac – top, CG\_Frac – middle, and Gon\_Frac – bottom). The upper panels show the monthly transpiration sums (in different colors); the lower panels show fractional contributions of water of a certain age/origin (by month) to the monthly transpiration sums.

### 3.2 Braud et al. (2009a) dataset analysis

#### 3.2.1 Parameter optimization and model performance

The global sensitivity analysis and Monte-Carlo filtering results for the Braud et al. (2009a) dataset are shown in the Results S2 section of the Supplementary material. The most sensitive parameters were shape parameters  $n$  and saturated water contents  $\theta_s$ . The final optimized soil hydraulic and solute transport parameters and corresponding KGEs are shown in Table 3. Considering (or not) evaporation fractionation also impacted parameter estimation significantly. The most significant impacts were on dispersivity,  $\lambda$ , and the shape parameter,  $\alpha$  (Table 3). The soil water retention curves (Fig. S12) showed that the wilting points

were almost identical for the Non\_Frac and fractionation (CG\_Frac, Gon\_Frac, Meas\_Frac) scenarios. However, the saturated water contents were higher, and water contents started to drop later in the fractionation scenarios than those in the Non\_Frac scenario. The soil hydraulic conductivity curves (Fig. S12) showed that the saturated hydraulic conductivities were very similar, but the hydraulic conductivities in the fractionation scenarios were a little higher than those in the Non\_Frac scenario.

The fits of soil profile isotopic compositions for different fractionation scenarios are shown in Fig. 9. The Non\_Frac scenario had an almost uniform isotopic composition profile. In this case, the parameter optimization depended mainly on the measured soil water content profile. In fractionation scenarios, the peak value of the isotopic composition profile in the Meas\_Frac scenario was smaller than those in the Gon\_Frac and CG\_Frac scenarios, while the value of dispersivities was the opposite. Different fractionation scenarios resulted in significantly different average fitting performances (KGE\_avg) (reached 0.72). The Meas\_Frac scenario had the highest KGE\_wi (i.e., for soil water isotopic composition), followed by Gon\_Frac and CG\_Frac scenarios, while the Non\_Frac scenario performed the worst. The difference between KGE\_wi indices for different fractionation scenarios reached 1.49.

Table 3. Optimized parameters and Kling-Gupta efficiency (KGE) indices (wc, wi, and avg refer to the water content, water isotopic composition, and average, respectively) for different fractionation scenarios (Non\_Frac, CG\_Frac, Gon\_Frac, and Meas\_Frac) (for the Braud et al. (2009a) dataset).

Fractionation scenario	$\theta_r$ cm <sup>3</sup> /cm <sup>3</sup>	$\theta_s$ cm <sup>3</sup> /cm <sup>3</sup>	$\alpha$ (cm <sup>-1</sup> )	$n$ (-)	$K_s$ (cm/d)	$\lambda$ (cm)	KGE_wc	KGE_wi	KGE_avg
Non_Frac	0	0.435	0.0103	2.352	0.158	0.166	0.96	-0.55	0.20
CG_Frac	0	0.458	0.0106	2.367	0.139	0.126	0.85	0.37	0.61
Gon_Frac	0	0.441	0.0101	2.352	0.142	0.114	0.96	0.47	0.71
Meas_Frac	0	0.452	0.0082	2.392	0.156	0.932	0.90	0.94	0.92

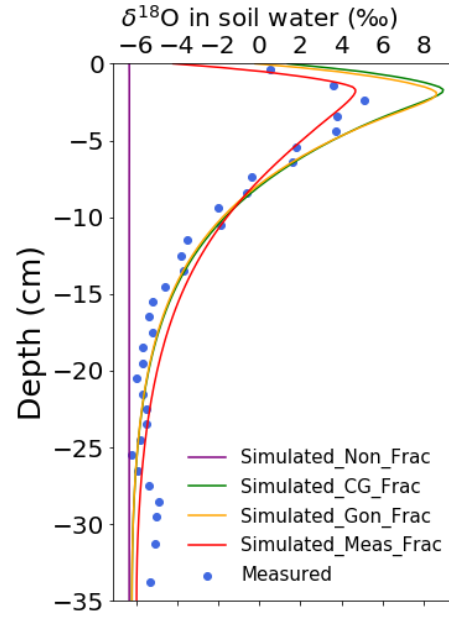


Figure 9. Measured (symbols) and simulated (lines)  $\delta^{18}\text{O}$  isotopic compositions across the soil profile for different fractionation (Non\_Frac, CG\_Frac, Gon\_Frac, and Meas\_Frac) scenarios (for the Braud et al. (2009a) dataset).

### 3.2.2 Second practical application: Estimation of evaporation flux

Table 4 shows cumulative evaporation obtained using different measurements and simulated considering different fractionation scenarios. The average isotopic composition of the whole profile was calculated using soil water contents and the column depth as weights. Cumulative evaporation was estimated to account for about 64.4%, 63.1%, and 65.6% of the initial soil water storage in the CG\_Frac, Gon\_Frac, and Meas\_Frac scenarios, respectively. These values for the CG\_Frac, Gon\_Frac, and Meas\_Frac scenarios were (slightly) lower than but comparable to laboratory measurements and the HYDRUS-1D water balance. Slight differences may have been caused by uncontrollable measurement errors in the isotopic composition of the atmospheric water vapor ( $\delta_a$  in Eq. 5), which is the most sensitive parameter in the isotope mass balance method (Skrzypek et al., 2015). Cumulative evaporation cannot be estimated using this method in the Non\_Frac scenario since no isotopic enrichment occurred (i.e.,  $\delta_s = \delta_0$  in Eq. 4).

Table 4. Cumulative evaporation measured using different experimental methods and calculated considering different fractionation scenarios.

Method	Fractionation scenario	Cumulative evaporation (mm)	Initial soil water storage (mm)	$F_E$ (-)
Direct measurement (of airflow and humidity)		105	153	68.7%
Column weighting		103	153	67.1%
Trapped volume		103	153	67.3%
HYDRUS-1D water mass balance	Non_Frac	105	151	69.5%
	CG_Frac	105	159	66.0%
	Gon_Frac	105	153	68.6%
	Meas_Frac	105	157	66.9%
Isotope mass balance	Non_Frac	-	151	-
	CG_Frac	102	159	64.4%
	Gon_Frac	97	153	63.1%
	Meas_Frac	103	157	65.6%

Note that values of cumulative evaporation for the first three laboratory measurement methods are from Braud et al. (2009a).

## 4 Discussion

### 4.1 Impacts of evaporation fractionation on parameter estimation and model performance

For the Stumpp et al. (2012) dataset, as indicated in Section 3.1.1, the fractionation scenarios (CG\_Frac and Gon\_Frac) had lower hydraulic conductivities than the Non\_Frac scenario. This is because fractionation decreases the isotope flux by evaporation compared with a no fractionation scenario (the isotopic composition of the evaporation flux cannot be greater than that of surface soil water) and thus increases the isotope flux by net infiltration. To get a good fit between simulated and observed isotopic compositions of discharge water, the inverse modeling yields a larger longitudinal dispersivity (to increase the dispersion of isotopes) (Table 1) or lower hydraulic conductivities (to decrease downward convection of isotopes) (Fig. S8).

The simulated isotopic composition of the lysimeter discharge remained the same for different fractionation scenarios during about the first 150 d and started deviating after this time (Fig. 6). This suggests

that it takes about 150 d before the impact of different treatments of the upper BC for isotope transport propagates to the soil profile bottom and affects the isotopic composition in drainage water (Zhou et al., 2021). This time interval (i.e., about 150 d) is much smaller than the travel time of the first particle (released at the soil surface) as calculated by the particle tracking method (Fig. S9). This is because the particle tracking algorithm considers only piston flow, while dispersion accelerates the arrival of isotopes to the soil profile bottom. However, the trends are still similar, except for some vertical shifts.

Since KGE<sub>wi</sub> values did not differ much for different fractionation scenarios (within 0.09) (Fig. 6 and Table 1), considering (or not) evaporation fractionation does not significantly impact the isotopic composition in discharge water in this example (humid conditions). The Non\_Frac scenario had a slightly higher KGE<sub>wi</sub>, indicating that it can fit isotopic data better, followed by CG\_Frac, while Gon\_Frac performed the worst. This is understandable since evaporation fractionation could be neglected in this example, as seen from the dual-isotope plots (Fig. 5 of Stumpp et al., 2012).

For the Braud et al. (2009a) dataset, as indicated in Section 3.2.1, the hydraulic conductivities in the fractionation (CG\_Frac, Gon\_Frac, Meas\_Frac) scenarios were a little higher than those in the Non\_Frac scenario. This is because fractionation decreases the isotope flux by evaporation compared with a no fractionation scenario. A higher hydraulic conductivity in the fractionation scenarios promotes upward evaporation and fractionation. This increases the isotopic composition of remaining soil water and thus produces a better fit between simulated and observed isotope profiles.

When evaporation fractionation was not considered, the isotopic composition of evaporation remained the same as the initial isotopic composition. This resulted in a uniform isotopic composition (equal to the initial value) distribution of soil water throughout the profile in the Non\_Frac scenario (Fig. 9). In fractionation scenarios, the peak value of the isotopic composition profile was inversely proportional to the dispersivity value (Fig. 9 and Table 3), which is consistent with the conclusions from Braud et al. (2009b).

The isotopic composition profiles and the KGE<sub>wi</sub> values differed dramatically (reached 1.48) between different fractionation scenarios (Fig. 9 and Table 3). This implies that considering evaporation

fractionation significantly impacts the isotopic composition profile in this example (arid conditions). The Meas\_Frac scenario had the highest KGE\_wi (i.e., for the water isotopic composition), followed by the Gon\_Frac, and then CG\_Frac, while the Non\_Frac scenario performed the worst. This is understandable since evaporation fractionation could not be neglected, and the measured evaporation isotope flux is the most accurate for this example (Braud et al. 2009b).

## **4.2 Impacts of evaporation fractionation on practical applications**

### **4.2.1 Estimation of drainage and RWU travel times**

Differences in water travel times were not evident among different fractionation scenarios (Table 4), since the numerator in Eq. 2 is much larger than the denominator in the peak displacement method. As a result, water travel times were similar for different fractionation scenarios despite a very different dispersivity. However, for the particle tracking method based on water flow calculations, differences in water travel times were evident among different fractionation scenarios (Table 2), despite their similar KGE values (Table 1). In addition, differences in estimated soil hydraulic parameters may also cause discrepancies in *TTs* of individual precipitation events and the temporal origin of water for RWU (Figs. S8 and 7~8).

Overall, the particle tracking method gave much higher travel times than the peak displacement method (Table 2). Different results by these two methods may be associated with different rainfall events selected for these calculations. The peak-displacement method calculates the travel times during frequent and heavy precipitation events (precipitation events from 2005~2006), while particle tracking assesses the travel times over longer periods (Zhou et al., 2021).

Notably, water travel times in the Non\_Frac scenario obtained by the particle tracking method are most consistent with the approximate estimate of 41 weeks provided by previous studies with similar crops and areas (Stumpp et al., 2009). It is worth mentioning that Asadollahi et al. (2020) pointed out that the SAS approach was a good alternative for estimating water travel times when the system was too complicated to be fully described by the HYDRUS-1D model. Our study demonstrates that the water-flow-based particle

tracking module in HYDRUS-1D is another promising way of constraining estimation errors in water travel times, especially when there is not enough isotope data to calibrate the lumped or physically based isotope transport models.

In contrast, considering fractionation using either the CG or Gonfiantini models will likely led to larger water travel time estimates than in the Non\_Frac scenario (Table 2). This is because fractionation scenarios result in a larger dispersivity (to increase the dispersion of isotopes) or lower hydraulic conductivities (to decrease convection of isotopes), as discussed in Section 4.1.

#### **4.2.2 Estimation of the evaporation flux**

For evaporation estimation, the isotope-transport-based methods for different fractionation (CG\_Frac, Gon\_Frac, and Meas\_Frac) scenarios can give comparable results to the water-flow-based methods, including laboratory measurements and the HYDRUS-1D water balance. In contrast, the Non\_Frac scenario can produce similar results only when using the water-flow-based method (HYDRUS-1D water balance). However, since the measured evaporation flux was used as the upper boundary condition in this (arid conditions) example, it is not clear whether the similarity between estimated evaporation amounts using the HYDRUS-1D water balance method in the Non\_Frac and fractionation (CG\_Frac, Gon\_Frac, Meas\_Frac) scenarios was due to this boundary condition, or because actual soil hydraulic conductivities and water contents were continuously adjusted to actual soil fluxes without ever reaching full saturation. However, it is clear that evaporation fractionation has a significant impact on the isotope transport and isotopic compositions in arid conditions, as shown in Fig. 9. Therefore, the direct use of simulated isotopic compositions in the Non\_Frac scenario may result in large biases in practical applications in arid conditions, as seen from the evaporation estimation results in Table 4.

#### **4.3 Comparison of different climate conditions and implications for future studies**

The soil saturated hydraulic conductivities ( $K_s$ ), and the retention curve shape parameter ( $\alpha$ ) were the parameters most affected by the consideration of evaporation fractionation for the humid condition dataset (Table 1). For the arid condition dataset, these were the dispersivity ( $\lambda$ ) and the retention curve shape



parameter ( $\alpha$ ) (Table 3). This is likely associated with the effects of soil texture on retention curves and soil moisture conditions in different climate zones (Radcliffe and Šimůnek, 2018). Overall, soil water retention and hydraulic conductivity curves (Fig. S12) in different fractionation scenarios were more similar for the Braud et al. (2009a) dataset than the Stumpp et al. (2012) dataset (Fig. S8). One reason is that the measured evaporation flux was used as the upper BC in the former, which constrains the model flexibility. Another reason is that there was only one soil layer in the Braud et al. (2009a) dataset, while there were three soil layers in the Stumpp et al. (2012) dataset. There is likely a compensation effect between the parameters of different layers, and thus the parameter values can vary more in the Stumpp et al. (2012) dataset.

While evaporation fractionation plays an essential role in parameter estimation in both cases, its impact on model performance is relatively small in the example for humid conditions but more significant in the example for arid conditions, as discussed in Sections 4.1 and 4.2. This is expected since evaporation plays a more important role in the water balance of the arid dataset (Table 4) than in the humid dataset (Fig. S13). These conclusions also indirectly validate the common assumption that evaporation fractionation may be neglected in some humid regions but not in arid areas (Sprenger et al., 2016a).

However, parameter sensitivities and optimization results reflect complex combined effects of climate, soil, and vegetation characteristics. The isotopic composition of soil water is not only affected by evaporation fractionation, but also by the mixing of rainfall with soil water and different flow paths in the soil, leading to its variations with depths and time. The insufficient knowledge of the spatiotemporal isotope distribution (e.g., in shallow and deep depths or during different stages of evaporation) and the lack of such information in the objective function may bias the parameter estimation results. For example, not including isotopes from different soil depths within the soil profile might lead to an underestimation of evaporation fractionation in general, biased estimation of water mixing within the profile, and a similar isotopic signal in the discharge. In this study, we considered either the time series of the isotopic composition of the bottom flux in the Stumpp et al. (2012) dataset or the final isotopic composition profile in the Braud et al. (2009a) dataset. In addition, observation data types and spatiotemporal distributions are different for these two

datasets, and this difference may affect the comparison of parameter estimation results between different climate conditions.

The GSA was carried out for the Non\_Frac scenario for the Stumpp et al. (2012) dataset and the Meas\_Frac scenario for the Braud et al. (2009a) dataset because they were closest to the experimental conditions. This implicitly assumes that sensitivity remains the same for different model structures. However, different model structures may affect GSA and PSO results, which should be further explored. Last but not least, the impacts of possible transpiration fractionation, as observed in multiple studies, should also be included in future analyses (e.g., Barbeta et al., 2019). Therefore, it is difficult to generalize the results of this study or apply them to other specific conditions.

## **5 Summary and Conclusions**

In this study, we analyzed parameter estimation results for two datasets collected under humid and arid climate conditions using the isotope transport model, in which we either did or did not consider evaporation fractionation. The global sensitivity analysis using the Morris and Sobol' methods and the parameter estimation using the Particle Swarm Optimization algorithm highlight the significant impacts of considering evaporation fractionation on parameter estimation and model performance. The KGE index for isotope data can increase by 0.09 and 1.49 for the humid and arid datasets, respectively, when selecting suitable fractionation scenarios.

The impact of different parameter values estimated when considering (or not) evaporation fractionation propagates into practical applications of isotope transport modeling. The isotope-transport-based method (peak displacement) gave much lower water travel times than the water-flow-based method (particle tracking) for humid conditions. Considering fractionation using the CG and Gonfiantini models will likely lead to larger water travel time estimates and ages for RWU. For arid conditions example, the isotope-transport-based method (isotope mass balance) can provide comparable evaporation estimates for different fractionation (CG\_Frac, Gon\_Frac, Meas\_Frac) scenarios as the water-flow-based methods

(HYDRUS-1D water balance and laboratory measurements). In contrast, the Non\_Frac scenario can produce reasonable evaporation estimation only when using the water-flow-based method.

The direct use of simulated isotopic compositions in the no fractionation scenario may result in large biases in practical applications in arid regions where evaporation fractionation is more extensive than in humid areas. Integrated use of water-flow and isotope-transport-based methods may provide mutual validation and be an important way to avoid this problem. This research may shed some light on future laboratory and field experimental designs regarding the practical applications of the isotope-transport modeling in different climate zones.

## Appendix

Acronym/Symbol	Description	Dimension/Units
$P$	Precipitation	L
$ET_0$	Grass-reference potential evapotranspiration	L
$E$	Actual evaporation	L
$E_i$	Isotope flux of evaporation	‰·L/T or $ML^{-2}/T$
$T_s$	Soil surface temperature	°C
$T_{air}$	Air temperature	°C
$RH$	Air relative humidity	-
$LAI$	Leaf area index	-
$\delta_P$	Isotopic composition of precipitation	‰
$\delta_0$	Initial isotopic composition of soil water	‰
$\delta_E$	Isotopic composition of evaporation flux	‰
$\delta_s$	Isotopic composition of the residual liquid	‰
$\delta^*$	Limiting isotopic composition	‰
$\delta_A$	Isotopic composition of the atmospheric water vapor	‰
$xm$	Enrichment slope	-
$\alpha^+$	Equilibrium fractionation factor	-
$\varepsilon^+$	Equilibrium fractionation enrichment	‰
$\varepsilon_k$	Kinetic fractionation enrichment	‰
$\alpha_i^k$	Kinetic fractionation factor at the soil surface	-
$\alpha_i^D$	Kinetic fractionation factor within the soil	-
$n_k$	Kinetic fractionation coefficient within the soil	-
$F_E$	Ratio of the evaporation loss to the initial water storage	-
$\theta_r$	Residual water content	$L^3/L^3$
$\theta_s$	Saturated water content	$L^3/L^3$
$n, \alpha$	Shape parameters of the VG model	-
$K_s$	Saturated hydraulic conductivity	L/T
$\lambda$	Longitudinal dispersivity	L

## Acknowledgments

This research was financially supported by the Multistate W4188 program. We acknowledge Paolo Benettin from the Laboratory of Ecohydrology ENAC/IEE/ECHO, École Polytechnique Fédérale de Lausanne (EPFL), Lausanne, Switzerland, for his useful suggestions. We also appreciate the editors and reviewers for their constructive comments on this manuscript.

## References

- Allen, S.T., Kirchner, J.W., Braun, S., Siegwolf, R.T.W., Goldsmith, G.R., 2019. Seasonal origins of soil water used by trees. *Hydrology and Earth System Sciences*, 23(2): 1199-1210. DOI:10.5194/hess-23-1199-2019
- Asadollahi, M., Stumpp, C., Rinaldo, A., Benettin, P., 2020. Transport and Water Age Dynamics in Soils: A Comparative Study of Spatially Integrated and Spatially Explicit Models. *Water Resources Research*, 56(3): 17. DOI:10.1029/2019wr025539
- Barbeta, A., Jones, S. P., Clavé, L., Wingate, L., Gimeno, T. E., Fréjaville, B., Wohl, S., and Ogée, J., 2019. Unexplained hydrogen isotope offsets complicate the identification and quantification of tree water sources in a riparian forest. *Hydrology and Earth System Sciences*, 23(4): 2129-2146. DOI:10.5194/hess-23-2129-2019
- Benettin, P., Bertuzzo, E., 2018. tran-SAS v1.0: a numerical model to compute catchment-scale hydrologic transport using StorAge Selection functions. *Geosci. Model Dev.*, 11(4): 1627-1639. DOI:10.5194/gmd-11-1627-2018
- Benettin, P., Rinaldo, A., Botter, G., 2015. Tracking residence times in hydrological systems: forward and backward formulations. *Hydrological Processes*, 29(25): 5203-5213. DOI:10.1002/hyp.10513
- Benettin, P., Volkmann, T. H. M., von Freyberg, J., Frentress, J., Penna, D., Dawson, T. E., and Kirchner, J. W., 2018. Effects of climatic seasonality on the isotopic composition of evaporating soil waters. *Hydrology and Earth System Sciences*, 22(5): 2881-2890. DOI:10.5194/hess-22-2881-2018
- Beven, K., Freer, J., 2001. Equifinality, data assimilation, and uncertainty estimation in mechanistic modelling of complex environmental systems using the GLUE methodology. *Journal of Hydrology*, 249(1-4): 11-29. DOI:10.1016/s0022-1694(01)00421-8
- Bouhlef, M.A., Bartoli, N., Otsmane, A. and Morlier, J., 2016. Improving kriging surrogates of high-dimensional design models by Partial Least Squares dimension reduction, *Struct. Multidiscip. Optim.*, 53(5), pp. 935-952, doi:10.1007/s00158-015-1395-9
- Braud, I., Bariac, T., Biron, P., Vauclin, M., 2009a. Isotopic composition of bare soil evaporated water vapor. Part II: Modeling of RUBIC IV experimental results. *Journal of Hydrology*, 369(1-2): 17-29. DOI:10.1016/j.jhydrol.2009.01.038
- Braud, I., Biron, P., Bariac, T., Richard, P., Canale, L., Gaudet, J. P., and Vauclin, M., 2009b. Isotopic composition of bare soil evaporated water vapor. Part I: RUBIC IV experimental setup and results. *Journal of Hydrology*, 369(1-2): 1-16. DOI:10.1016/j.jhydrol.2009.01.034
- Brinkmann, N., Seeger, S., Weiler, M., Buchmann, N., Eugster, W., and Kahmen, A., 2018. Employing stable isotopes to determine the residence times of soil water and the temporal origin of water taken up by *Fagus sylvatica* and *Picea abies* in a temperate forest. *New Phytologist*, 219(4): 1300-1313. DOI:10.1111/nph.15255
- Brunetti, G., Šimůnek, J., Piro, P., 2016. A comprehensive numerical analysis of the hydraulic behavior of a permeable pavement. *Journal of Hydrology*, 540: 1146-1161. DOI:10.1016/j.jhydrol.2016.07.030

- Brunetti, G., Šimůnek, J., Turco, M., Piro, P., 2018. On the use of global sensitivity analysis for the numerical analysis of permeable pavements. *Urban Water J.*, 15(3): 269-275. DOI:10.1080/1573062x.2018.1439975
- Brunetti, G., Šimůnek, J., Turco, M., Piro, P., 2017. On the use of surrogate-based modeling for the numerical analysis of Low Impact Development techniques, *Journal of Hydrology*, 548, pp. 263-277, doi:10.1016/j.jhydrol.2017.03.013
- Campolongo, F., Cariboni, J., Saltelli, A., 2007. An effective screening design for sensitivity analysis of large models. *Environ. Modell. Softw.*, 22(10): 1509-1518. DOI:10.1016/j.envsoft.2006.10.004
- Chesnaux, R., Stumpp, C., 2018. Advantages and challenges of using soil water isotopes to assess groundwater recharge dominated by snowmelt at a field study located in Canada. *Hydrological Sciences Journal*, 63(5): 679-695. DOI:10.1080/02626667.2018.1442577
- Condon, L.E., Atchley, A.L., Maxwell, R.M., 2020. Evapotranspiration depletes groundwater under warming over the contiguous United States. *Nature Communications*, 11(1): 8. DOI:10.1038/s41467-020-14688-0
- Craig, H., Gordon, L., 1965. Deuterium and oxygen 18 variations in the ocean and the marine atmosphere, *Stable Isotopes in Oceanographic Studies and Paleotemperatures E*, Proceedings of the Third Spoleto Conference, Spoleto, Italy, pp. 9-130.
- Gatel, L., Lauvernet, C., Carlier, N., Weill, S., Tournebise, J., and Paniconi, C., 2019. Global evaluation and sensitivity analysis of a physically based flow and reactive transport model on a laboratory experiment. *Environ. Modell. Softw.*, 113: 73-83. DOI:10.1016/j.envsoft.2018.12.006
- Gonfiantini, R., 1986. Environmental isotopes in lake studies. *Handbook of Environmental Isotope Geochemistry*, 2: 113-168.
- Groh, J., Stumpp, C., Lücke, A., Pütz, T., Vanderborght, J., and Vereecken, H., 2018. Inverse Estimation of soil hydraulic and transport parameters of layered soils from water stable isotope and lysimeter data. *Vadose Zone Journal*, 17(1): 19. DOI:10.2136/vzj2017.09.0168
- Harman, C.J., 2015. Time-variable transit time distributions and transport: Theory and application to storage-dependent transport of chloride in a watershed. *Water Resources Research*, 51(1): 1-30. DOI:10.1002/2014wr015707
- Herman, J., Usher, W., 2017. SALib: an open-source Python library for sensitivity analysis. *Journal of Open Source Software*, 2(9): 97. DOI:10.21105/joss.00097
- Herman, J.D., Kollat, J.B., Reed, P.M., Wagener, T., 2013. Technical Note: Method of Morris effectively reduces the computational demands of global sensitivity analysis for distributed watershed models. *Hydrology and Earth System Sciences*, 17(7): 2893-2903. DOI:10.5194/hess-17-2893-2013
- Hopmans, J.W., Šimůnek, J., Romano, N., Durner, W., 2002. 3.6. 2. Inverse Methods. *Methods of Soil Analysis: Part 4 Physical Methods*, 5: 963-1008.
- Knoben, W.J.M., Freer, J.E., Woods, R.A., 2019. Technical note: Inherent benchmark or not? Comparing Nash-Sutcliffe and Kling-Gupta efficiency scores. *Hydrology and Earth System Sciences*, 23(10): 4323-4331. DOI:10.5194/hess-23-4323-2019
- Koeniger, P., Gaj, M., Beyer, M., Himmelsbach, T., 2016. Review on soil water isotope-based groundwater recharge estimations. *Hydrological Processes*, 30(16): 2817-2834. DOI:10.1002/hyp.10775
- Liang, G., 1982. Net radiation, potential and actual evapotranspiration in Austria. *Archives for Meteorology, Geophysics, and Bioclimatology, Series B*, 31(4): 379-390.
- Liu, D., Li, L.Z., Rostami-Hodjegan, A., Bois, F.Y., Jamei, M., 2020. Considerations and caveats when applying global sensitivity analysis methods to physiologically based pharmacokinetic models. *AAPS J.*, 22(5): 13. DOI:10.1208/s12248-020-00480-x
- Mattei, A., Goblet, P., Barbecot, F., Guillon, S., Coquet, Y., and Wang, S., 2020. Can soil hydraulic parameters be estimated from the stable isotope composition of pore water from a single soil profile? *Water*, 12(2): 19. DOI:10.3390/w12020393
- Mertens, J., Stenger, R., Barkle, G.F., 2006. Multiobjective inverse modeling for soil parameter estimation and model verification. *Vadose Zone Journal*, 5(3): 917-933. DOI:10.2136/vzj2005.0117

- Miguez-Macho, G., Fan, Y., 2021. Spatiotemporal origin of soil water taken up by vegetation. *Nature*: 17. DOI:10.1038/s41586-021-03958-6
- Nelson, J.A., Pérez-Priego, O., Zhou, S., Poyatos, R., Zhang, Y., Blanken, P.D., Gimeno, T.E., Wohlfahrt, G., Desai, A.R., Gioli, B. and Limousin, J.M., 2020. Ecosystem transpiration and evaporation: Insights from three water flux partitioning methods across FLUXNET sites. *Glob. Change Biol.*, 26(12): 6916-6930. DOI:10.1111/gcb.15314
- Nossent, J., Elsen, P., Bauwens, W., 2011. Sobol' sensitivity analysis of a complex environmental model. *Environ. Modell. Softw.*, 26(12): 1515-1525. DOI:10.1016/j.envsoft.2011.08.010
- Penna, D., Hopp, L., Scandellari, F., Allen, S.T., Benettin, P., Beyer, M., Geris, J., Klaus, J., Marshall, J.D., Schwendenmann, L. and Volkmann, T.H., 2018. Ideas and perspectives: Tracing terrestrial ecosystem water fluxes using hydrogen and oxygen stable isotopes - challenges and opportunities from an interdisciplinary perspective. *Biogeosciences*, 15(21): 6399-6415. DOI:10.5194/bg-15-6399-2018
- Radcliffe, D.E., Šimůnek, J., 2018. *Soil physics with HYDRUS: Modeling and applications*. CRC Press.
- Ratto, M., Tarantola, S., Saltelli, A., 2001. Sensitivity analysis in model calibration: GSA-GLUE approach. *Comput. Phys. Commun.*, 136(3): 212-224. DOI:10.1016/s0010-4655(01)00159-x
- Razavi, S., A. Jakeman, A. Saltelli, C. Prieur, B. Iooss, E. Borgonovo, E. Plischke, S. Lo Piano, T. Iwanaga, W. Becker, S. Tarantola, J.H.A. Guillaume, J. Jakeman, H. Gupta, N. Melillo, G. Rabitti, V. Chabridon, Q.Y. Duan, X.F. Sun, S. Smith, R. Sheikholeslami, N. Hosseini, M. Asadzadeh, A. Puy, S. Kucherenko, and H.R. Maier, 2021. The future of sensitivity analysis: An essential discipline for systems modeling and policy support, *Environ. Modell. Softw.*, 137, pp. 22, doi:10.1016/j.envsoft.2020.104954
- Rinaldo, A., Benettin, P., Harman, C.J., Hrachowitz, M., McGuire, K.J., Van Der Velde, Y., Bertuzzo, E. and Botter, G., 2015. Storage selection functions: A coherent framework for quantifying how catchments store and release water and solutes. *Water Resources Research*, 51(6): 4840-4847. DOI:10.1002/2015wr017273
- Sheikholeslami, R., Razavi, S. and Haghnegahdar, A., 2019. What should we do when a model crashes? Recommendations for global sensitivity analysis of Earth and environmental systems models, *Geosci. Model Dev.*, 12(10), pp. 4275-4296, DOI:10.5194/gmd-12-4275-2019
- Shi, Y.H., Eberhart, R., 1998. A modified particle swarm optimizer, *IEEE International Conference on Evolutionary Computation*. Ieee, Anchorage, Ak, pp. 69-73. DOI:10.1109/icec.1998.699146
- Šimůnek, J., 1991. Numerical simulation of the transport processes in soil. *Vodohospodarsky Casopis (CSFR)*.
- Šimůnek, J., Šejna, M., Saito, H., Sakai, M., van Genuchten, M.T., 2008. *The HYDRUS-1D Software Package for Simulating the One-Dimensional Movement of Water, Heat, and Multiple Solutes in Variably Saturated Media*, Version 4.0. HYDRUS Software Series 3. Department of Environmental Sciences, University of California Riverside, Riverside, California, USA, 315 pp.
- Skrzypek, G., Mydlowski, A., Dogramaci, S., Hedley, P., Gibson, J. J., and Grierson, P. F., 2015. Estimation of evaporative loss based on the stable isotope composition of water using Hydrocalculator. *Journal of Hydrology*, 523: 781-789. DOI:10.1016/j.jhydrol.2015.02.010
- Sobol, I.M., 2001. Global sensitivity indices for nonlinear mathematical models and their Monte Carlo estimates. *Math. Comput. Simul.*, 55(1-3): 271-280. DOI:10.1016/s0378-4754(00)00270-6
- Sprenger, M., Leistert, H., Gimbel, K., Weiler, M., 2016a. Illuminating hydrological processes at the soil-vegetation-atmosphere interface with water stable isotopes. *Reviews of Geophysics*, 54(3): 674-704. DOI:10.1002/2015rg000515
- Sprenger, M., Seeger, S., Blume, T., Weiler, M., 2016b. Travel times in the vadose zone: Variability in space and time. *Water Resources Research*, 52(8): 5727-5754. DOI:10.1002/2015wr018077
- Sprenger, M., Volkmann, T.H., Blume, T., Weiler, M., 2015. Estimating flow and transport parameters in the unsaturated zone with pore water stable isotopes. *Hydrology and Earth System Sciences*.

- Stumpp, C., Maloszewski, P., Stichler, W., Fank, J., 2009. Environmental isotope ( $\delta^{18}\text{O}$ ) and hydrological data to assess water flow in unsaturated soils planted with different crops: Case study lysimeter station "Wagna" (Austria). *Journal of Hydrology*, 369(1-2): 198-208. DOI:10.1016/j.jhydrol.2009.02.047
- Stumpp, C., Stichler, W., Kandolf, M., Šimůnek, J., 2012. Effects of land cover and fertilization method on water flow and solute transport in five lysimeters: A long-term study using stable water isotopes. *Vadose Zone Journal*, 11(1): 14. DOI:10.2136/vzj2011.0075
- Sutanto, S.J., Wenninger, J., Coenders-Gerrits, A.M.J., Uhlenbrook, S., 2012. Partitioning of evaporation into transpiration, soil evaporation and interception: a comparison between isotope measurements and a HYDRUS-1D model. *Hydrology and Earth System Sciences*, 16(8): 2605-2616. DOI:10.5194/hess-16-2605-2012
- Timbe, E., Windhorst, D., Crespo, P., Frede, H. G., Feyen, J., and Breuer, L., 2014. Understanding uncertainties when inferring mean transit times of water through tracer-based lumped-parameter models in Andean tropical montane cloud forest catchments. *Hydrology and Earth System Sciences*, 18(4): 1503-1523. DOI:10.5194/hess-18-1503-2014
- Vrugt, J.A., Robinson, B.A., 2007. Improved evolutionary optimization from genetically adaptive multimethod search. *Proc. Natl. Acad. Sci. U. S. A.*, 104(3): 708-711. DOI:10.1073/pnas.0610471104
- Vrugt, J.A., Stauffer, P.H., Wohling, T., Robinson, B.A., Vesselinov, V.V., 2008. Inverse modeling of subsurface flow and transport properties: A review with new developments. *Vadose Zone Journal*, 7(2): 843-864.
- Wohling, T., Vrugt, J.A., 2011. Multiresponse multilayer vadose zone model calibration using Markov chain Monte Carlo simulation and field water retention data. *Water Resources Research*, 47: 19. DOI:10.1029/2010wr009265
- Wollschläger, U., Pfaff, T., Roth, K., 2009. Field-scale apparent hydraulic parameterisation obtained from TDR time series and inverse modelling. *Hydrology and Earth System Sciences*, 13(10): 1953-1966. DOI:10.5194/hess-13-1953-2009
- Zhou, T., Šimůnek, J., Braud, I., 2021. Adapting HYDRUS-1D to simulate the transport of soil water isotopes with evaporation fractionation. *Environ. Modell. Softw.*, 143: 18. DOI:10.1016/j.envsoft.2021.105118